AGU100 ADVANCING EARTH AND SPACE SCIENCE

JGR

Journal of Geophysical Research: Oceans

RESEARCH ARTICLE

10.1029/2018JC013765

Key Points:

- Local wind and ambient current forcing combine to alter the plume momentum balance, resulting in less spreading and mixing under NW winds
- This plume reconfiguration results in larger net mixing under NW winds, when low local mixing rates act over a larger mixing region
- The plume is largely unaffected by the estimated wave-driven effects on its dynamics and mixing

Correspondence to:
S. E. Kastner,
skastner@uw.edu

Citation:
Kastner, S. E., Horner-Devine, A. R., & Thomson, J. (2018). The influence of wind and waves on spreading and mixing in the Fraser River plume. *Journal of Geophysical Research: Oceans*, *123*, 6818–6840. https://doi.org/10.1029/2018JC013765

Received 9 JAN 2018
Accepted 27 AUG 2018
Accepted article online 5 SEP 2018
Published online 22 SEP 2018

The Influence of Wind and Waves on Spreading and Mixing in the Fraser River Plume

Samuel E. Kastner[1], **Alexander R. Horner-Devine**[1], **and Jim Thomson**[2]

[1]Department of Civil Engineering, University of Washington, Seattle, WA, USA, [2]Applied Physics Lab, University of Washington, Seattle, WA, USA

Abstract This study uses drifter-based observations to investigate the role of wind and waves on spreading and mixing in the Fraser River plume. Local winter wind patterns commonly result in two distinct forcing conditions, moderate winds from the southeast (SE) and strong winds from the northwest (NW). We examine how these patterns influence the spreading and mixing dynamics of the plume. Under SE winds, the plume thins, spreads, and turns to the right (north) upon exiting the river mouth. Mixing is initially intense in the region of maximum spreading, but it is short-lived. Under NW winds, which oppose the rightward tendency of the plume, the plume remains thicker, narrower, and flows directly across the Strait with a lateral front on its northern side. Mixing is initially lower than under SE forcing but persists further across the Strait. A Lagrangian stream-normal momentum balance shows that wind and interfacial stress under NW conditions compress the sea surface height anomaly formed by the river discharge and guide the flow across the Strait. This reconfiguration changes spreading and mixing dynamics of the plume; plume spreading, which drives intense mixing under SE winds, is shut down under NW winds, and mixing rates are consequently much lower. Despite the initially lower mixing rates, the region of active mixing extends further under NW winds, resulting in higher net mixing. These results highlight that the wind, which is often a primary cause of increased plume mixing, can also significantly influence mixing by changing the geometry of the plume.

Plain Language Summary Rivers transport sediment, pollutants, and nutrients from inland regions to coastal seas. Where rivers meet the ocean, freshwater flows over the ambient salty seawater, forming a river plume. The quantities that the river transports into the ocean are mixed into the seawater along with the freshwater, and so it is vital to understand this mixing process. While ocean surface waves might be the most striking visual feature of the coastal ocean, at the Fraser River mouth, south of Vancouver, Canada, we find that wind is a much more important influence on river plume mixing than waves. Wind can influence mixing by changing the geometry of the plume to either favor or discourage intense mixing occurring in the system. This is a result of the wind encouraging or discouraging plume spreading, which is the primary cause of mixing close to the river mouth. Ocean surface waves, despite being a visually striking feature of this system, do not play a large role in mixing the Fraser River plume. Thus, in order to correctly predict river plume mixing, we must take into account wind conditions near the river mouth, while waves are less important.

1. Introduction

River outflows are ubiquitous features of coastal waters. An important objective of river plume studies is to understand and predict the processes leading to mixing of the plume with seawater since this controls the dispersal of river-borne sediments, nutrients, and contaminants along the coast. In this paper, we investigate the processes by which local winds influence plume mixing. We show that the wind's dynamical influence on plume spreading significantly modifies mixing and that this effect may be of equal or greater magnitude than wind mixing due to direct input of turbulence and shear at the surface.

Much attention has been devoted to understanding plume mixing driven by spreading and shear in the near field and midfield of the plume structure (Hetland, 2010; MacDonald & Geyer, 2004; McCabe et al., 2008; Yuan & Horner-Devine, 2013, 2017) and wind-driven mixing due to Ekman processes in the far field (Fong & Geyer, 2001; Lentz, 2004). An underlying assumption of most near-field dynamics studies has been that the wind is relatively unimportant in this region (Chen et al., 2009; Kilcher et al., 2012; McCabe et al., 2009). Some studies have examined the impact of wind and wave forcing on the dynamics of plumes in the far field (Akan et al., 2017; Lentz & Largier, 2006), and many have studied wave-driven turbulence in the open ocean (Craig & Banner, 1994; Gemmrich, 2010; Thomson et al., 2016); however, the effects of wind and wave forcing on near-field plume mixing are not well understood (Kakoulaki et al., 2014).

1.1. Plume Mixing and Spreading

Plume mixing is typically strongest in the near-field region, with associated turbulent kinetic energy (TKE) dissipation rate values as high as 10^{-3} m^2/s^3 (Kilcher et al., 2012; MacDonald & Geyer, 2004; MacDonald et al., 2007). Mixing and turbulence in this region is caused by increased velocity shear as the fresh river water spreads from its source and lifts off the bottom. Spreading causes the buoyant layer to shoal and accelerate (Garvine, 1984; Hetland, 2010). The competition between the generation of turbulence due to velocity shear and the suppression of turbulence due to density stratification is characterized in terms of the Richardson number,

$$Ri = \frac{g'}{\rho_0} \frac{\partial \rho / \partial z}{(\partial u / \partial z)^2} , \tag{1}$$

where $g' = g(\rho_{\mathrm{salt}} - \rho_{\mathrm{plume}})/\rho_0$ is the reduced gravity specific to the stratification, ρ_0 is a reference density, ρ is fluid density, u is the fluid velocity, and z is the vertical coordinate. Increased shear causes the local Richardson number to decrease and mixing and turbulence to intensify to a peak value seaward of the liftoff point (MacDonald et al., 2007; McCabe et al., 2008). Entrainment of low-momentum, high-density ambient water subsequently decreases the shear present in the surface plume layer and increases the Richardson number. However, as river water exits the mouth, it is no longer laterally constrained and spreads. In large-scale plumes, spreading is predominantly controlled by a competition between the stream-normal pressure gradient and Coriolis force, as shown by Garvine (1987) and later confirmed in the field by (McCabe et al., 2009; hereafter MC09). In order for mass to be conserved, the plume speeds up and thins as it spreads, thereby increasing shear. Thus, as the plume expands, its fate is determined by the competition between acceleration due to spreading and deceleration due to mixing (Garvine, 1984; Hetland, 2010; Horner-Devine et al., 2015). As the aspect ratio of a river plume is typically small ($h_p/L = \mathcal{O}(10^{-3})$, where h_p is the depth of the plume and L is the horizontal length scale of the plume, most mixing occurs via the vertical turbulent flux of density through the base of the plume (Luketina & Imberger, 1987, 1989; McCabe et al., 2008). As the plume spreads, its base area increases, increasing the area over which mixing can occur (Yuan & Horner-Devine, 2013). Observations of the near-field Merrimack River plume show that spreading can also be described by the stretching of a Kelvin-Helmholtz instability along its rotational axis, leading to a relationship between plume spreading and mixing (MacDonald & Chen, 2012). This theory matches recent observations from the Connecticut River estuary (Geyer et al., 2017).

Plume spreading is intrinsically related to the plume momentum balance. Spreading takes several forms in plume studies. An early study by Wright and Coleman (1971) shows analytically that the plume front spreads at a speed $2c$, where c is the internal wave phase speed associated with the plume stratification. Garvine (1984) shows that truly radial spreading can result in a ring structure due to mixing in the interior of the plume. Including the effects of Earth's rotation yields slightly different results (Garvine, 1987; McCabe et al., 2009). MC09 show that spreading of water parcels in a river plume is an asymmetric process due to Coriolis. Their model results of the Columbia River plume show the formation of a dome of freshwater offshore of the river mouth on ebb tide, resulting in a stream-normal pressure gradient that is symmetrical about the center axis of the plume near the river mouth. This pressure gradient by itself would force symmetrical plume spreading. However, as the plume moves offshore, it is affected by Coriolis, which pushes the entire plume to the right and results in asymmetrical spreading on each side of the plume. On the right side, Coriolis and the pressure gradient work in concert to enhance spreading, and on the left side, Coriolis and the pressure gradient work against each other to limit spreading. In this paper we will examine the effects of variable spreading on mixing and use its implications for plume dynamics to infer the shape of the plume.

The dominant terms of the plume momentum balance vary across the spatial scales of a river plume (Garvine, 1984; Hetland, 2005; Horner-Devine et al., 2009, 2015). Modeling and analytical studies have shown that near the river mouth, the stream-normal momentum balance is controlled by centrifugal, stream-normal pressure gradient and Coriolis forces (Garvine, 1987; McCabe et al., 2009). In a numerical model of the Merrimack River plume, Chen et al. (2009) add that interfacial shear stress may affect plume spreading close to the river mouth. The streamwise momentum balance has been shown to be dominated by the streamwise pressure gradient and advection with interfacial shear stress divergence the dominant cause of plume deceleration (Garvine, 1987; Kilcher et al., 2012).

1.2. Wind-Driven Plume Processes

Wind has generally been assumed to have a secondary effect on mixing in energetic plume regions such as the near field and is often neglected in near-field mixing studies. Dynamical studies, however, have long included local winds as an important plume forcing mechanism (Csanady, 1978; Chao, 1988b), typically focusing on Ekman dynamics caused by alongshore winds (Csanady, 1978; Chao, 1988b; Fong et al., 1997; Masse & Murthy, 1990). Chao, (1988a, 1988b) shows in a numerical model that downwelling winds enhance the formation of a buoyant coastal current, while upwelling winds limit this behavior, increase the seaward excursion of the plume, and decrease stratification. Horner-Devine et al. (2009) show similar results from observations of the Columbia River plume, where wind can stop the accumulation of water in the bulge region. In the far field, wind-driven plume mixing has been characterized as an Ekman-driven process (Chao, 1988b; Fong & Geyer, 2001). Numerical models show upwelling wind can mix a plume of uniform depth to a critical depth set by Ekman transport, mass conservation, and the critical bulk Richardson number while spreading the plume offshore (Fong & Geyer, 2001). Once the far-field plume reaches this critical depth, mixing is suppressed. A dye release experiment compares well to this formulation of wind-driven mixing (Houghton et al., 2004). Modifications to this model show similar behavior in the presence of more complex geometry and at larger scales using analytical and numerical techniques (Lentz, 2004; Hetland, 2005). Lentz and Largier (2006) expand this model to apply to downwelling winds, showing that downwelling winds pin the plume to the coast, leading to a vertically mixed but still relatively fresh water mass, with inhibited mixing relative to upwelling winds. These modifications compare well to the results of Fong and Geyer (2001) and observations from the Chesapeake Bay buoyant coastal current.

Close to the river mouth and with cross-shore winds, wind forcing can drive advection of the plume in the direction the wind is blowing. Advection and mixing in the Hudson River plume can be changed by the diurnal sea breeze, particularly under neap tide and strong discharge conditions when the plume is shallow and highly stratified (Hunter et al., 2010). The sea breeze traps the Hudson plume by the Long Island coast, where it forms a recirculating bulge. Chao (1988b) shows similar results from a numerical model, in which a plume forced by landward winds is trapped near the coast. Observations by Hickey et al. (1998) of the Columbia River plume close to the river mouth indicate that the plume may be advected north or south by corresponding winds. Similarly, drifters show that the Merrimack River plume is strongly affected in its near field and midfield by moderate wind forcing (>4 m/s), responding in the direction of the wind present (Kakoulaki et al., 2014).

Wind and ambient currents have also been shown to advect plumes and alter plume shape on various geometrical scales. Using an analytical solution, Garvine (1982) shows that an ambient current can bound plume spreading by forming a lateral front perpendicular to the direction of the current, causing the plume velocity to turn downstream (relative to the ambient current). O'Donnell (1990) uses a numerical model to show that higher ambient current crossflow velocities result in a deeper plume layer near the river mouth and that in this case, mixing only mildly modifies the plume structure.

1.3. Wave-Driven Processes

Breaking waves are a significant source of near-surface oceanic turbulence (Craig & Banner, 1994; Melville, 1996; Terray et al., 1996). A controlling parameter in wave breaking processes is wave steepness, conventionally defined as $(H_{\mathrm{sig}}k_p)/2$ (Banner et al., 2000). An increase in steepness due to wave-current interaction leads to observed increased wave breaking at the Columbia River plume front (Zippel & Thomson, 2017), and it has been suggested that the resulting turbulence could conceivably mix the plume (Thomson et al., 2014). In the presence of following or opposing currents, waves are lengthened or shortened, respectively. In wave-current interaction, the absolute wave frequency ω is conserved such that

$$\omega = \sigma + \vec{u} \cdot \vec{k}, \tag{2}$$

where $\vec{u}$ is the current, k is the wavenumber, and σ is the intrinsic frequency from the linear dispersion relation $\sigma^2 = gktanh(kd)$, with d being the depth. It can be shown analytically that waves are blocked by an opposing current when the group velocity of the waves $c_g = \frac{\partial\omega}{\partial k} \leq -u$, where u is the current speed (Mei, 1989). However, waves typically break due to a limiting steepness at much lower current speeds, $u < c_g/2$(Chawla & Kirby, 2002).

Breaking waves impart a momentum flux through the water surface, known as the radiation stress, in addition to a flux of turbulence. Radiation stress gradients release momentum to the mean water level or mean currents. This process is commonly observed to cause wave set up and currents very close to shore (Longuet-Higgins, 1970; Longuet-Higgins & Stewart, 1961; Thornton & Guza, 1986).

Surface wave breaking over the far-field plume leads to a thicker, narrower, and more vertically homogeneous plume than would be expected under upwelling wind conditions (Gerbi et al., 2013). Model simulations of plumes with wave breaking also show more intense mixing than those without; these simulations also show that the analytical framework from Lentz (2004) underpredicts the rate of plume thickening in simulations with wave breaking (Gerbi et al., 2013; Rong et al., 2014). Gerbi et al. (2015) examine the thickening rate under wind and wave forcing using a one-dimensional numerical model and show that surface wave breaking can hasten the thickening of a fresh surface layer (such as a far-field plume), especially when rotational effects are considered.

Recent studies have begun to address the effects of wave influence closer to the river mouth. Observations of the Columbia River plume show that the plume front is capable of blocking an opposing wind sea and that turbulence is elevated when this occurs (Thomson et al., 2014). Wave-breaking turbulence that is downwelled at the plume front could elevate the levels of turbulence at the plume base, leading to increased mixing. Waves may also have an impact on the plume momentum balance. Numerical modeling of the Columbia River plume shows that waves can shift the location of the plume hundreds of meters in the down-wave direction due to Stokes drift-driven horizontal advection (Akan et al., 2017).

Turbulence due to wave breaking is typically associated with dissipation rate values of $\mathcal{O}(10^-3)$ at the near surface; this turbulence is found to decay in magnitude exponentially beneath the surface (Gemmrich, 2010; Terray et al., 1996; Thomson et al., 2016). The turbulent dissipation rate associated with wave forcing, ϵ^{wave}, scales with a depth normalized by the wave height as $(z/H_{\text{sig}})^{-\lambda}$, where $-2 < \lambda < -1$, and a TKE flux G at the surface (Terray et al., 1996). This flux, which functions as the surface boundary condition for the turbulence, has been found to scale with the wind friction velocity, such that $G \sim u_*^3$ in deep water (Craig & Banner, 1994; Gemmrich, 2010). A scaling for G based on wave energy flux gradient dF/dx, H_{sig}, depth d, and an exponential function of normalized depth compares well with observations in shallow water (Feddersen, 2012; Zippel & Thomson, 2015).

2. Observational Program

2.1. Outline

The present work evaluates the wind and wave processes in the near-field Fraser River plume. Section 2 provides an overview of the Fraser River plume and our sampling plan. Section 3 details the methods used to analyze plume momentum, spreading, and mixing. Section 4 provides the results of momentum, spreading, and mixing calculations under different wind conditions. Section 5 addresses the implications of the results on the plume shape, the role of waves in the system, and the total mixing of the plume.

2.2. Geographical Setting and Conditions

The Fraser River drains an area of greater than 230,000 km^3 in western British Columbia, Canada, and is one of the longest river systems in the country at 1,370 km. Its highest flows of around 10,000 m^3/s (measured at Hope, BC) occur during the June freshet, and low flows ranging from 500 to 1,000 m^3/s occur between February and April. The river flows into the Strait of Georgia approximately 20-km south of Vancouver, over a network of tidal flats that are exposed at low water (Figure 1a). A jetty extends to the western edge of these tidal flats at Sand Heads (10-km offshore at high water) on the northern side of the river channel, which is maintained by dredging to a depth of 10 m (Figure 1a). Cutting off the channel from the surrounding water, the tidal flats and the jetty combine to make Sand Heads the effective river mouth (MacDonald & Geyer, 2005). The channel bends SW at a right angle at the 4-km marker in the channel, forcing the outflow to exit the channel in an approximately southwesterly direction. At the time of peak tidal discharge from the river, the tidal currents in the Strait of Georgia are southeasterly, resulting in an ambient current perpendicular to the river discharge.

Tides in the Strait of Georgia are primarily composed of a mixture of semidiurnal and diurnal constituents. During our sampling period, tidal amplitudes ranged from approximately 1 to 4 m (Figure 1d). Tidal currents recorded at Puffin Island Light south of the Fraser River mouth were as high as 0.5 m/s on both flood and ebb

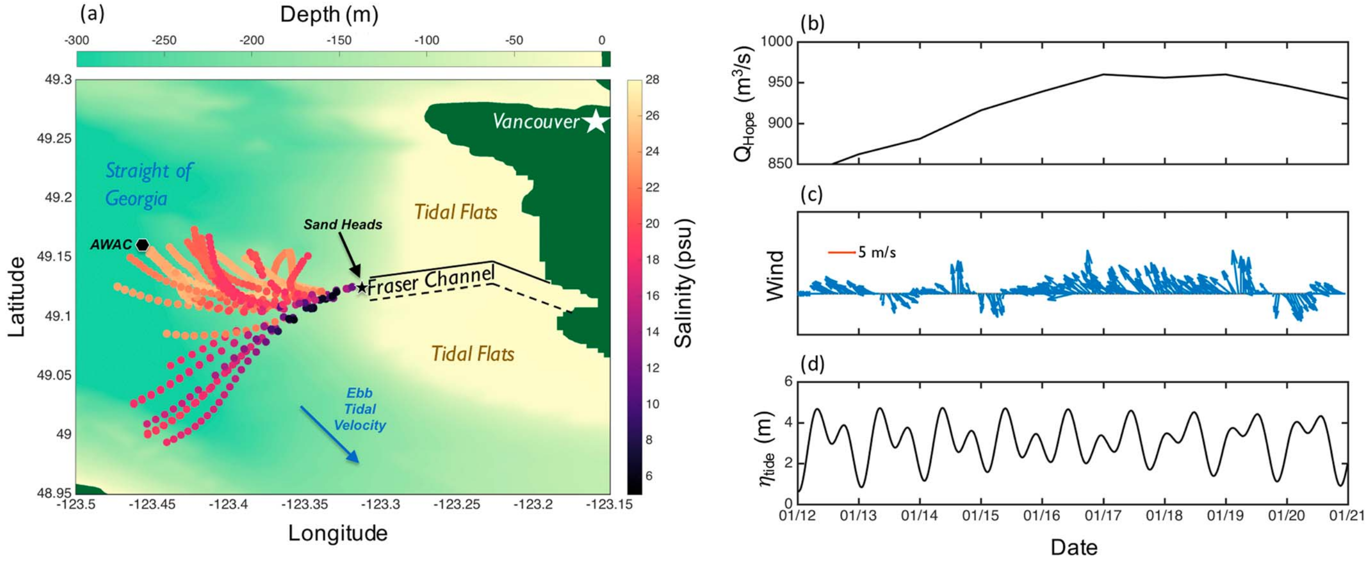

Figure 1. Drifter behavior and regional climate during the study period. (a) shows Surface Wave Instrument Float with Tracking drift tracks between 16 and 20 January, when Surface Wave Instrument Floats with Tracking were released from the river mouth. Points are colored by 0.5-m salinity measurements, and background color shows depth. Sand Heads is located at the seaward end of the Fraser Channel. The solid black line to the north of the Fraser Channel is the Sand Heads Jetty; the dashed black line on the south side of the channel is the approximate boundary of the tidal flats where channel dredging begins. The ebb tidal velocity in the Strait is noted as a blue arrow; (b)–(d) are time series during the study period of (b) discharge from the Fraser River at Hope gauging station (Environment Canada), (c) median Sand Heads wind speeds and directions for each day and (d) tidal stage, Sand Heads station (Environment Canada). AWAC = Acoustic Waves and Currents.

(Puffin Island Light lies south of the region shown in Figure 1a). The ebb tidal current is directed to the southeast, toward the Straits of Juan de Fuca. At the river mouth, we observed surface currents varying from 1.5 to 2.5 m/s at maximum ebb tide. During the lower flow conditions of winter, we observed the fresher surface flow at Sand Heads to have a characteristic salinity between 4 and 15 practical salinity unit (psu) depending on discharge. We observed this fresh layer to always be detached from the bottom at Sand Heads near max ebb, unlike the summer period analyzed in MacDonald and Geyer (2004).

In the winter, wind conditions in the Strait of Georgia are close to bimodal. Weak to moderate winds (5–7 m/s) out of the southeast are the predominant condition; however, winter storms in the region cause episodic strong northwest winds (10 m/s; Figure 1c). The fetch to the river mouth at Sand Heads under NW wind conditions is longer on average than under SE wind conditions due to the quasi-elliptical geometry of the Strait. The longer fetch and strong winds result in larger waves at Sand Heads under NW wind conditions.

During our study period, the Fraser River streamflow gauge at Hope, BC, measured discharges varying between 850 and 960 m^3/s, with larger discharges toward the end of the study (Figure 1b). This coincides with larger daylight ebbs, as the tidal phase shifted over the course of the study by ~6.5 hr (Figure 1d).

Our observations show wind speed variation between 3 and 10 m/s from a variety of wind directions (Figure 1c). Under stronger forcing (>5 m/s, 16–20 January), the wind was primarily from the SE, E, and NW. The resulting wave conditions under SE and NW winds follow the fetch relationship outlined above, with larger waves under NW winds (Table 1).

2.3. Measurements

We took measurements in the southern Strait of Georgia between 12 and 21 January 2016. Our ship-based observations were taken from the *R/V Jack Robertson* (University of Washington Applied Physics Lab), and we released Surface Wave Instrument Float with Tracking (SWIFT) drifters (Thomson, 2012) to perform Lagrangian observations under ebb tidal conditions. We placed an Acoustic Waves and Currents (AWAC) mooring to the NW of the river mouth to measure wave height and surface currents upstream (relative to the tidal current in the Strait) of the plume. Its location was to the north of the region pictured in Figure 1a.

Our deployments used two SWIFT models: the version 3 models, which are fully instrumented buoys, and the prototype version 4, which has reduced instrumentation. The version 3 SWIFTs collect conductivity and temperature data using either one or three Aanderaa 4319 sensors, mounted on the drifters' hulls at depths of

Table 1
Wind, Wave, Tidal, and Discharge Conditions

Parameter	17 January 2016	19 January 2016
Tidal amplitude (m)[a]	2.89	3.3
Hours after high water	4.25	5.3
Mean wind speed (m/s)[b]	7.2	8.4
Max wind speed (m/s)	9.2	12.3
Mean wind direction (° N)	127	284
Significant wave height (m)	0.7	1.1
Peak wave direction (° N)	104	317
River discharge (m^3/s)[c]	956	946

[a] Tidal conditions from Sand Heads (Environment Canada), hours after high water indicates time of deployments. [b] Wind and wave conditions from Surface Wave Instrument Floats with Tracking. [c] Discharge from Fraser at Hope gauging station (Environment Canada).

0.5 m or 0.2, 0.5, and 1.2 m, respectively. The version 3 measures wave spectra and bulk properties using either its GPS or Inertial Measurement Unit; the GPS is also used to calculate position, drift speed, and drift direction. The SWIFT's hull-mounted Nortek Aquadopp acoustic Doppler current profiler (ADCP) can be used to measure either velocity shear (downlooking configuration, 1-MHz narrowband mode) or near-surface turbulent dissipation rate using a structure function method (uplooking configuration, 2-MHz pulse-coherent *HR* mode). SWIFT drifters use an internal sampling protocol that yields five approximately 10-min data collection bursts each hour.

The prototype version 4 SWIFT (SWIFTv4β) uses a downlooking Nortek Signature (1 MHz) ADCP to measure velocity and turbulence profiles, including the TKE dissipation rate (Paris & Thomson, 2017). We also equipped the SWIFTv4β with two GPS units used to measure position, drift speed, and drift direction. During the deployments explored in this paper, we deployed a chain of up to six YSI Sonde 600LS conductivity-temperature-depths (CTDs) attached to the version 4 at 0.5-, 1.5-, 2-, 3-, 4-, and 5-m depth.

On 17 and 19 January, we repeated a similar deployment routine. Three pairs of SWIFTs were deployed each day, starting just before max ebb for 4–6 hr, in three cross-channel positions 200 m apart, just upstream of Sand Heads. One pair was deployed on the right side of the channel, one in the center, and one on the left side of the channel (Figures 2a and 2b). Most pairs included one uplooking SWIFT and one downlooking SWIFT, with one of these having three conductivity-temperature (CT) sensors. Specific instrumentation is detailed in Table 2. The SWIFTv4β was deployed in a different position on each day. On 17 January, the SWIFTv4β was deployed in the center of the channel, whereas on 19 January, it was deployed on the right side of the channel but was recovered before the other SWIFTs. Casts from the shipboard CTD were used to supplement its CTD chain for plume depth measurements. On 17 January, under SE winds, the pair of SWIFTs released on the right side of the channel was caught in an anomalous feature over the tidal flats north of Sand Heads, and so data from these SWIFTs are not included in this work.

The Robertson was equipped with two ADCPs: a pole-mounted RDI 1,200-kHz ADCP and a hull-mounted RDI 300-kHz ADCP. To capture density changes, we performed casts using a Seabird 19plus CTD and recorded surface salinity using a pole-mounted Aanderaa 4319 CT sensor. In this paper, we occasionally use the CTD

Table 2
Drifter Pair Instrumentation

Drifter pair	S1		S2		N1		N2		N3	
SWIFT	A	B	A	B	A	B	A	B	A	B
Number of CTs[a]	1	3	1	1	1	1	1	3	1	3
ADCP[b]	Up	Up	Up	Down	Up	Down	Up	Up	Down	Up

Note. SWIFT = Surface Wave Instrument Float with Tracking; ADCP = acoustic Doppler current profiler.
[a] Number of Aanderaa 4319 CT sensors onboard the SWIFT. [b] SWIFT Nortek Aquadopp look direction: "Up" indicates uplooking; "Down" indicates downlooking.

to supplement drifter data, while the shipboard ADCP data are used exclusively for contextual information (Figure 3).

3. Methods

3.1. Momentum Balance

In order to effectively understand the plume dynamics, we calculate momentum balances in a streamwise versus stream-normal reference frame (Garvine, 1987; Hench & Leuttich, 2003; McCabe et al., 2009). Our methods are similar to those described in Hench and Leuttich (2003) and MC09; however, the dynamics we expect from the Fraser system are different from the inlet dynamics described in Hench and Leuttich (2003) due to the presence of stratification and lack of bottom attachment of the plume (McCabe et al., 2009). Our calculations differ from those of MC09 in that our measurements are in the Lagrangian reference frame, so we derive a new set of *s*-*n* momentum equations using the appendix of Hench and Leuttich (2003). We neglect horizontal viscous terms, as we are not able to resolve these with our localized Lagrangian drifter measurements, and the small aspect ratio of the plume ($\frac{h}{L} \approx 10^{-3}$) suggests that they will be small. We integrate these equations vertically over the depth of the 21 psu isohaline to find the momentum balance in the buoyant layer,

$$0 = \overbrace{h_i \frac{DU_s}{Dt}}^{\substack{\text{streamwise}\\ \text{Lagrangian}\\ \text{acceleration}}} + \overbrace{\frac{h_i}{\rho_{\text{ref}}}\frac{\partial P}{\partial s}}^{\substack{\text{streamwise}\\ \text{pressure}\\ \text{gradient}}} - \overbrace{\frac{\tau_0^s - \tau_i^s}{\rho_{\text{ref}}}}^{\substack{\text{streamwise}\\ \text{stress}\\ \text{divergence}}} + \overbrace{\frac{(\tau_0^n - \tau_i^n)(\alpha_0 - \alpha_i)}{\rho_{\text{ref}}}}^{\substack{\text{normal stress}\\ \text{contribution through}\\ \text{vertical veering}}}, \tag{3}$$

$$0 = \underbrace{h_i U_s \frac{D\alpha}{Dt}}_{\substack{\text{rotational}\\ \text{Lagrangian}\\ \text{acceleration}}} + \underbrace{h_i f U_s}_{\substack{\text{Coriolis}\\ \text{acceleration}}} + \underbrace{\frac{h_i}{\rho_{\text{ref}}}\frac{\partial P}{\partial n}}_{\substack{\text{stream-normal}\\ \text{pressure}\\ \text{gradient}}} - \underbrace{\frac{\tau_0^n - \tau_i^n}{\rho_{\text{ref}}}}_{\substack{\text{stream-normal}\\ \text{stress}\\ \text{divergence}}} - \underbrace{\frac{(\tau_0^s - \tau_i^s)(\alpha_0 - \alpha_i)}{\rho_{\text{ref}}}}_{\substack{\text{streamwise stress}\\ \text{contribution through}\\ \text{vertical veering}}}, \tag{4}$$

where subscripts i and 0 denote the 21 psu isohaline (*interface* hereafter) and near-surface values, respectively. Subscript s denotes a streamwise variable, $\frac{\partial}{\partial s}$ and $\frac{\partial}{\partial n}$ denote streamwise and stream-normal partial derivatives, respectively, and $\frac{D}{Dt}$ indicates the total Lagrangian time derivative in the SWIFT reference frame. Thus, h_i indicates interfacial depth, U_s is the streamwise velocity, ρ_{ref} is a reference density taken as 1,021 kg/m^3 (S = 26 psu, T = 5 °C), P is pressure, τ is a stress applied in the streamwise or stream-normal direction at either the surface or the interface, and α is the direction of the streamline at either the near surface or interface. Since we make these calculations over a surface plume layer that we assume to have a uniform value of velocity, we take α to be constant with depth such that $\alpha_0 = \alpha_i = \alpha_{\text{mean}}$. We thus neglect the vertical veering terms in equations (3) and (4).

We calculate stream-normal momentum balances from pairs of SWIFTs released together. We only make momentum balance calculations for the pair of SWIFTs closest to the SWIFTv4β each day. Below, we describe our decomposition of the momentum equation into forcing terms for the acceleration, Coriolis, wind stress, and interfacial shear stress. We calculate pressure gradient as a residual term. Acceleration, Coriolis, and wind stress are taken to be the means of these terms for a SWIFT pair, while interfacial shear stress is calculated for SWIFTs with a downlooking ADCP. Wave radiation stress gradient and ambient current form drag are calculated using a mixture of data sources, as described below.

To calculate rotational Lagrangian acceleration, we take $h_i U_s$ as the vertical integral of velocity from the surface to the depth of the 21 psu isohaline, using downlooking ADCP velocity data from SWIFTs v4β and 09 (for SE and NW conditions, respectively) combined with SWIFT drift speed to create a profile of velocity to integrate. The error associated with picking a value of h_i from the interpolated SWIFT v4β CTD profile is included in the error propagation analysis detailed at the end of this subsection. The value $\frac{D\alpha}{Dt}$ is calculated as the time derivative of SWIFT drift direction.

We calculate the Coriolis acceleration by taking the value of $h_i U_s$ already found and multiplying it by the Coriolis parameter $f \approx 1.1 \times 10^{-4}$ for 49.1° N latitude.

To calculate the surface stress, we first assume that the wind stress is the only stress applied to the surface of the plume, such that $\tau_0 = \rho_a C_d U_{10}^2$, where $\rho_a = 1.225$ kg/m^3 is the density of air, $C_d = 1.5 \times 10^{-3}$ is a typical sea-surface drag coefficient, and U_{10} is the velocity at 10 m. We calculate U_{10} based on SWIFT wind measurements at 1-m height by extrapolating our measurements using an assumed wind speed log layer.

Similarly, we assume that shear stress is the only stress applied to the plume interface. We take the interfacial shear stress as $\tau_i = \rho_0 C_{di} \Delta u^2$, where ρ_0 is the density of the surface plume layer (taken from each SWIFT's CT measurement), Δu^2 is the difference between the velocity in the surface plume layer and the velocity just below the 21 psu isohaline, calculated from downlooking SWIFT current profiles, and C_{di} is the interfacial drag coefficient. Following Jurisa et al. (2016), the interfacial drag coefficient is expressed as

$$C_{di} = Ri_b^{3/2} \frac{(Ri_b^{-1} - Ri_c^{-1})(Ri_b^{-1/2} - Ri_c^{-1/2})}{96}, \tag{5}$$

where the critical bulk Richardson number is assumed to be $Ri_c = 1$. This parameterization is based on the kinetic energy available to create a turbulent overturn and the time scale related to the growth rate of Kelvin-Helmholtz instabilities and is consistent with Jurisa et al. (2016). Using a critical bulk Richardson number threshold dictates that we do not calculate a drag coefficient for subcritical bulk Richardson number and thus do not calculate a stress.

To mitigate the noise and error in the momentum terms above, we smooth measurements of water velocity, salinity, and wind velocity using a Butterworth filter. Smoothing removes along-track variability from both instrument error and small-scale processes that we do not aim to resolve in this paper, allowing us to analyze the larger-scale trends visible over the course of a drift track. Error propagation analysis allows us to estimate the resultant error in our momentum term estimates from this fitting.

As we do not directly resolve all stream-normal forcing on the system, we calculate a residual as the stream-normal momentum required to balance the rotational acceleration, Coriolis, interfacial shear stress, and wind stress terms. In sections 3.1.1 and 3.1.2, we detail methods used to estimate other forces that may have contributed to this residual. We then assume that the difference between the residual and these terms is the unresolved pressure gradient.

Two terms receive special attention in sections 4 and 5: the ambient current form drag and wave radiation stress gradient in the stream-normal momentum balance. We use the methods below to estimate these momentum contributions.

3.1.1. Wave Momentum Estimate

Wave forcing on the plume can be incorporated in the momentum balance as a horizontal gradient of wave radiation stress due to wave breaking at the plume front provided that we have good measurements of the radiation stress inside and immediately outside the plume front. The stream-normal radiation stress, S_{nn}, is the momentum flux carried by the waves and can be calculated as

$$S_{nn} = \rho g \int E(f). * \left(\frac{2k(f)d}{\sinh(2k(f)d)} + \frac{1}{2} \right) df, \tag{6}$$

where ρ is the water density, $E(f)$ is the spectral wave energy at a given frequency, f is wave frequency, $k(f)$ is the wave number at a given frequency, and d is water depth (Longuet-Higgins & Stewart, 1962). In order to compute a gradient of S_{nn}, we assume that waves are breaking and losing momentum flux across a front of width equal to two wavelengths as we observed from the deck of the *R/V Robertson*. Our measurements were conducive to making this estimate on 19 January 2016, which is the clearest example of the NW wind forcing studied in this paper. To calculate S_{nn}^{out}, the radiation stress outside of the plume, we use data from the first 10-min average recorded by SWIFT 11, which was deployed outside of the front. Over the course of the approximately 2-hr deployment, the front overtook the drifter; thus, we use only the initial data. We use data from SWIFT 15, deployed inside the plume to estimate S_{nn}^{in}. Assuming a steady wave field outside the plume during the deployment, we calculate $M_{\mathrm{wave}}^{n} = \frac{\partial S_{nn}}{\partial n} = \frac{S_{nn}^{\mathrm{out}} - S_{nn}^{\mathrm{in}}}{n_{\mathrm{front}}}$, where $n_{\mathrm{front}} \approx 50$ m is approximately two wavelengths of the incoming wave field.

Most error in this calculation comes from our estimates of the width of the lateral front. In subsequent calculations of M_{wave}^{n}, we calculate error assuming a factor of two variability in the width of the front, resulting in a factor of two variability in M_{wave}^{n}.

3.1.2. Ambient Current Form Drag Estimate

We observed a significant (60 cm/s) ambient surface current in the Strait of Georgia under NW winds, likely resulting from the superposition of a wind-driven current and the southeastward ebb tidal velocity. To incorporate this effect into our momentum balance (M_{ambient}), we make a simple control volume momentum conservation calculation. On the upstream (with respect to the ambient flow) end of the control volume, the current has an average velocity u_1 over a depth $H = 10$ m, set by the shear layer in Figures 3c and 3d. On the downstream end, the current has an average velocity u_2 over a depth $H - h$, where h is the thickness of the surface plume layer with the plume velocity directed perpendicular to the ambient current. If no momentum was lost due to the interaction with the plume layer, conservation of momentum shows that $u_1^2 H = u_2^2(H-h)$. Thus, a momentum input through the current form drag on the plume, M_{ac}^n, may be calculated such that

$$M_{ac}^n = \frac{u_1^2 H}{B} - \frac{u_2^2(H-h)}{B}, \tag{7}$$

where B is an effective length of the plume, taken as 17 km, the furthest extent of drifter deployments under NW winds.

The above formulation for M_{ac}^n assumes that the ambient current in the Strait is perpendicular to the plume streamlines, which is approximately true for NW winds. As this is the only wind condition for which we can calculate M_{ac}^n due to the location of our measurements, effects of the angle of incidence are neglected. As stated in section 3.1, we subtract our calculations of M_{ac}^n and M_{wave}^n from the residual to better infer the pressure gradient under NW winds.

To characterize the error associated with M_{ambient}, we use physically intuitive bounds on the control volume. The lower bound is characterized by the case where $u_1 = u_2$, in which $M_{\text{ambient}} = 0$. The upper bound is given by the case where $u_2 = 0$, which yields a maximum M_{ambient} for a given u_1.

Including the above terms in equation (4), we can redefine the stream-normal momentum balance such that

$$\begin{aligned} 0 \quad &= \underbrace{h_i U_s \frac{D\alpha}{Dt}}_{\substack{\text{rotational}\\\text{Lagrangian}\\\text{acceleration}}} + \underbrace{\frac{h_i}{\rho_{\text{ref}}}\frac{\partial P}{\partial n}}_{\substack{\text{stream-normal}\\\text{pressure}\\\text{gradient}}} - \underbrace{\frac{\rho_a C_d U_{10}^2}{\rho_{\text{ref}}}}_{\substack{\text{stream-normal}\\\text{wind}\\\text{stress}}} \\ &+ \underbrace{\frac{\rho_0 C_{di} \Delta u^2}{\rho_{\text{ref}}}}_{\substack{\text{stream-normal}\\\text{interfacial}\\\text{shear stress}}} + \underbrace{\frac{S_{nn}^{\text{out}} - S_{nn}^{\text{in}}}{n_{\text{front}}}}_{\substack{\text{Wave}\\\text{radiation stress}\\\text{gradient}}} + \underbrace{\frac{u_1^2 H - u_2^2(H-h)}{B}}_{\substack{\text{Ambient}\\\text{current}\\\text{form drag}}}. \end{aligned} \tag{8}$$

We make this calculation for one pair of drifters under each condition. For SE winds, we use SWIFT pair S1 (Figure 2a). For NW winds, we use SWIFT pair N1, which appear as one drift track due to their close proximity (Figure 2b).The SWIFTv4β was also used to provide downlooking current profiles for the SE wind condition. Note that pair S1 was released in the center of the channel, and pair N1 was released to the right (north) side of the channel. These drifters were chosen due to their initial deployment position, as they were the closest drifters to the stratification measurements made by the SWIFTv4β.

3.2. Spreading

Following MC09, we determine spreading, B_{tot}, for a drifter pair as the integral in time of

$$d\vec{U} = \vec{U}_b - \vec{U}_a = \frac{D\vec{B}}{Dt} = \sqrt{U_b^2 + U_a^2 - 2U_b U_a \cos(\alpha_b - \alpha_a)}, \tag{9}$$

where dU is the difference between the velocity vectors of the drifters along a drift track, U is the drifter speed, α is the drift direction, and subscripts a and b indicate a specific drifter in the pair.

MC09 show that spreading can be caused by differences in drift angle or by differences in speed between drifters a and b. In order to define the component of spreading caused by differences in speed, we may calculate $B_{\Delta U}$ by taking the difference between the drift speeds of the drifter pair, such that $B_{\Delta U} = U_2 - U_1$.

By subtracting $B_{\Delta U}$ from B_{tot}, we may calculate $B_{\Delta\alpha}$, the component of spreading caused by differences in drift angle. Each spreading component is related to a directional momentum balance, with $B_{\Delta U}$ caused by stream-normal differences in the streamwise momentum balance between a pair of drifters, and $B_{\Delta\alpha}$ is caused by the resultant acceleration of the the stream-normal momentum balance. Thus, by calculating $B_{\Delta U}$ and $B_{\Delta\alpha}$, it is possible to discern whether the streamwise or stream-normal momentum balance is the predominant cause of plume spreading.

Similarly to our momentum balance calculations, we fit spreading values using a cubic polynomial along each track. Fitting smooths along-track variability from both instrument error and small-scale processes that we do not aim to resolve in this paper, allowing us to analyze the larger-scale trends visible over the course of a drift track. Error propagation analysis allows us to estimate the resultant error in our spreading terms calculations.

3.3. Mixing

Previous work by MacDonald and Geyer (2004) and McCabe et al., 2008 (2008; hereafter, MC08) establishes a control volume formulation based on salt conservation to calculate salt flux through the base of the plume. MC08 establishes the following relationship for a Lagrangian plume measurement:

$$S_e w_e = \frac{1}{B}\frac{\partial}{\partial s}(uhBS), \tag{10}$$

where $S_e w_e$ is the salt flux through the bottom of the control volume (described as an entrained salinity, S_e, multiplied by the entrainment velocity, w_e, at the plume base), u is the velocity of the plume water, B is the distance between the drifters, h is the depth of the base of the slab layer, S is a representative plume salinity, and $\frac{\partial}{\partial s}$ represents the derivative in the streamwise direction. This calculation is based upon several assumptions. First, the plume system must be reasonably approximated by a slab of fresher water flowing over an ambient saltier layer. Second, the velocities must be steady over a given streamwise interval. Third, there must be no lateral contributions to mixing.

We use SWIFT drift speed as plume velocity u, SWIFT 0.5-m salinity as S, and the separation between a pair of coreleased SWIFTs as B. The 0.5-m CT measurement from each SWIFT is a valid representation of the plume salinity, as it is the freshest plume water that could mix with the water below. In order to find a representative h, we combine salinity measurements from the CTD chain attached to the SWIFT v4β and near-surface salinity from SWIFTs with three CTs. The combination of these measurements gives us information about salinity down to 4 m. After vertical interpolation and smoothing, we pick h as the depth of the 21 psu isohaline. While the surface plume water is continuously stratified, the depth of the 21 psu isohaline appears to be a point of inflection for the vertical salinity and velocity structure (Figure 3) under both conditions and is consistently observed by our salinity measurements over the length of deployments on each day. Thus, $S_e = 21$. This allows us to assume the plume behaves as a two-layer slab model. We do observe slight variability of S and u between drifters in a pair and therefore smooth the mean S and u values of the two drifters before calculating the mixing; we also use the pair's smoothed B values and the plume-wide smoothed value of h. We calculate streamwise gradients relative to the length of the drifter track for a 10-min SWIFT data burst; we thus assume that the plume is steady over the course of a 10-min period. Previous studies using SWIFT drifters have shown that SWIFTs are very close to a Lagrangian platform (Thomson, 2012). We can thus assume that the SWIFTs trace out streamlines over the course of a 10-min data collection burst and that there are no unaccounted-for lateral contributions to mixing.

In a similar manner to our momentum balance calculations, we fit salinity, velocity, plume depth, and spreading to a cubic polynomial with respect to the drifter track length to account for noise in our mixing estimate. Fitting smooths over along-track variability from both instrument error and small-scale processes that we do not aim to resolve in this paper, allowing us to analyze the larger-scale trends visible over the course of a drift track. Error propagation analysis allows us to estimate the resultant error in our mixing estimate from fitting.

For comparison with other turbulence parameters, the measured salt flux can be expressed as a TKE dissipation rate ϵ^{salt} according to

$$\epsilon^{\mathrm{salt}} = \frac{\beta g S_e w_e}{\Gamma}, \tag{11}$$

where $\beta = \frac{\partial\rho}{\partial S}$ is the change in density with salinity, and $\Gamma = 0.2$ is the mixing efficiency (McCabe et al., 2008; Peltier & Caulfield, 2003).

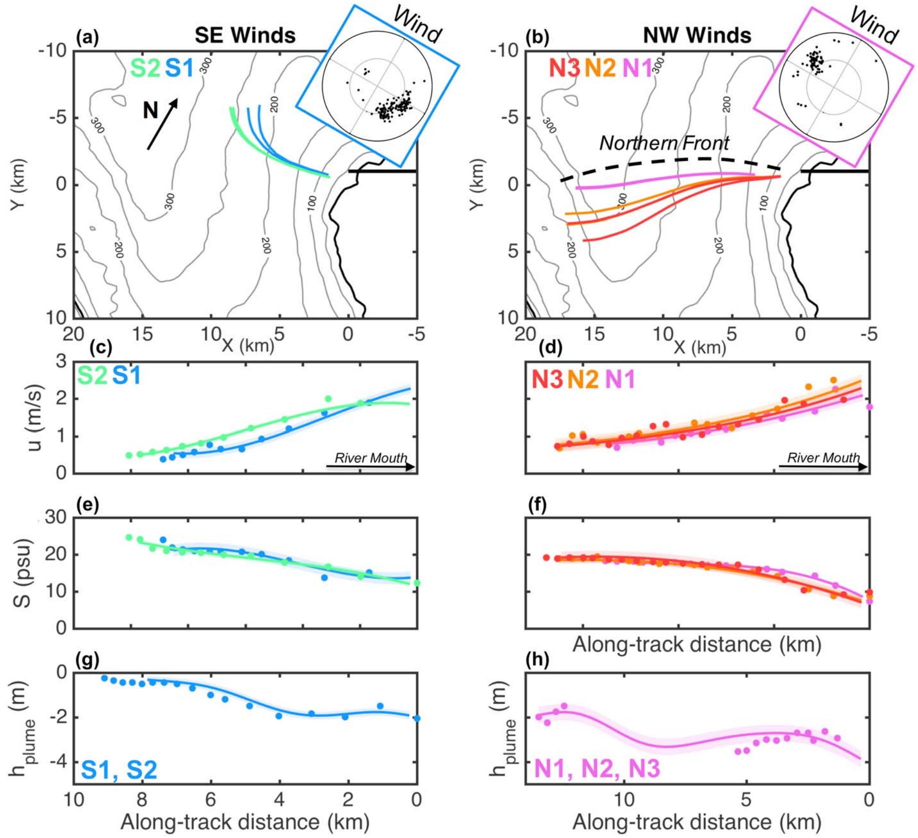

Figure 2. Wind speed and direction, Surface Wave Instrument Float with Tracking drifter tracks, velocities, salinities, and plume depth for SE and NW winds. Colors of drift tracks and along-track properties match for an indicated drifter pair. (a) and (b) show Surface Wave Instrument Float with Tracking measured wind speed and direction, along with drifter tracks and bathymetry for the Strait of Georgia. The inner wind speed ring is 5 m/s; the outer ring is 10 m/s. Wind speed and direction polar plots are tilted to be in the same reference frame as the maps, with north indicated as indicated in (a). The wind direction indicated is the direction the wind is from. The thin solid black line is the western boundary of the tidal flats near Sand Heads. The thick solid black line is the Sand Heads jetty. An approximate northern front is notated as a black-dotted line on (b). Labels (i.e., S1 and N1) indicate the name of a drifter pair; (c) and (d) show along-track drift speed values, raw (points) and smoothed with a 95% confidence interval; (e) and (f) show along-track salinity values, raw (points) and smoothed with a 95% confidence interval; (g) and (h) show along-track values of the 21 psu isohaline, one per day, raw (points) and smoothed with a 95% confidence interval. Note that for SE winds, the maximum along-track distance is 8 km, and for NW winds, the maximum along-track distance is 15 km. For all along-track plots, along-track distance increases to the left to match the maps, with the river mouth at the origin on the right, as noted in (c) and (d).

4. Results

4.1. Observed Plume Behavior

The trajectories of the drifters released at Sand Heads are shown in Figure 1a. Two overall behaviors are observed: drifters that curve northward upon exiting the river mouth and drifters that transit almost directly across the Strait. As discussed in section 2.2, wind forcing tends to be either from the SE or the NW in the winter, and the two observed plume behaviors coincide with these differing forcing conditions. In order to examine the plume response, we focus our analysis on two days that offer the clearest examples of these two dominant wind patterns: 17 and 19 January 2016, which corresponded to SE and NW winds, respectively (Table 1 and Figure 2). Table 1 shows that discharge, tidal stage, deployment time relative to high tide, and mean wind speed between the days are similar, while maximum wind speed, wind direction, and the resulting significant wave height and direction differ. On 17 January, the SWIFTs reported a mean maximum wind speed of 7 m/s out of the southeast, and on 19 January, a wind speed of 8 m/s out of the northwest (see Table 1). The discharge and tidal amplitude were similar on each day, and we deployed drifters just after max ebb. These winds resulted in larger wave heights under NW winds conditions and a corresponding change in wave direction.

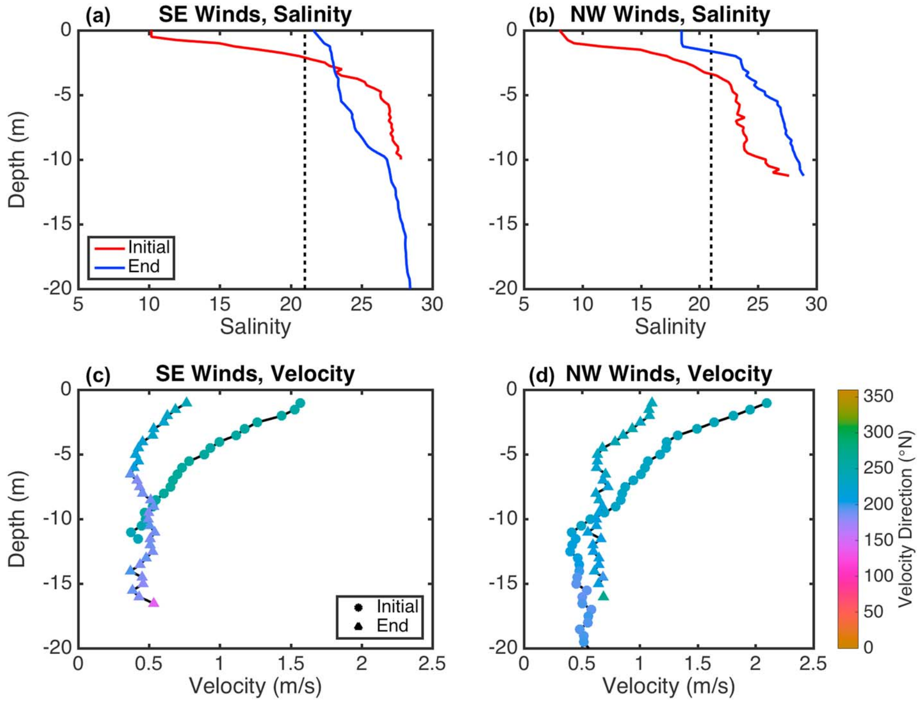

Figure 3. Profiles of salinity and velocity for the beginning and end of drift tracks for each condition. (a) and (b) show salinity profiles for SE and NW winds, respectively. Red lines indicate initial conditions, and blue lines indicate conditions at the end of the drift near the drifter recover location. (c) and (d) show velocity profiles for SE and NW winds, respectively, from the shipboard acoustic Doppler current profiler. Circle markers indicate initial profiles, and triangle markers indicate profiles from the end of a drift near the drifter recovery location. Color indicates velocity direction in degrees from north. On each day, the initial and end profiles were taken about 2.5 hr apart, at the start and end of drifter deployments.

4.2. Plume Response to SE and NW Winds

The wind and wave conditions experienced under SE and NW wind conditions resulted in contrasting plume behaviors, as observed in drift speed, salinity, and isohaline depth characteristics (Figures 2c–2h). Overall, the plume under NW winds (pairs N1, N2, and N3) was faster, fresher, and deeper than the plume under SE winds (pairs S1 and S2). The drift speed was similar at Sand Heads for each condition, but higher drift speeds persisted for longer under NW winds. Additionally, under SE winds, the drift speed at the end of the deployment was 0.5 m/s, but under NW winds was 1 m/s. Salinity increased at a similar rate under each condition, but the initial salinity was higher under SE winds. This variation in initial salinity may be due to variability in estuarine mixing during previous tidal cycles and advection of saltier water off of the tidal flats into the Fraser channel due to the SE wind; the Sand Heads jetty would block this process under NW winds. Under NW winds, we observed the lateral northern front of the plume in the ship's radar due to the high intensity of wave breaking along the front (radar not shown; schematic in Figure 2b). The higher seaward excursion under NW winds is similar to the upwelling wind condition modeled by Chao (1988b), although on length scales roughly one order of magnitude smaller.

Velocity profiles collected from the shipboard ADCP show different current structure under the two wind conditions. Under SE winds, the near-surface velocity near the river mouth is 1.5 m/s in a sheared layer approximately 4 m thick (Figure 3c). The velocity is directed to the southwest, across the Strait, following the trajectory of the Sand Heads jetty. Soon after the drifters exit the river mouth, the surface layer velocity turns to the north, as would be expected as a result of Coriolis acceleration. As it turns, the layer slows and thins to a depth of approximately 1 m, consistent with the decreasing depth of the 21 psu isohaline observed by the SWIFTv4β. By the end of the deployment, the velocity is 10% of its initial value. Beneath the surface layer, there is a smaller flow toward the south associated with the ebb tidal current in the Strait of Georgia. Under NW winds, the near-surface velocity starts at 2 m/s and forms a sheared layer that is approximately 6 m thick (Figure 3d). This velocity is directed across the Strait, controlled by the channel at Sand Heads during the beginning of the drift track, but stays directed roughly southwest throughout the entire deployment. The surface layer stays thicker

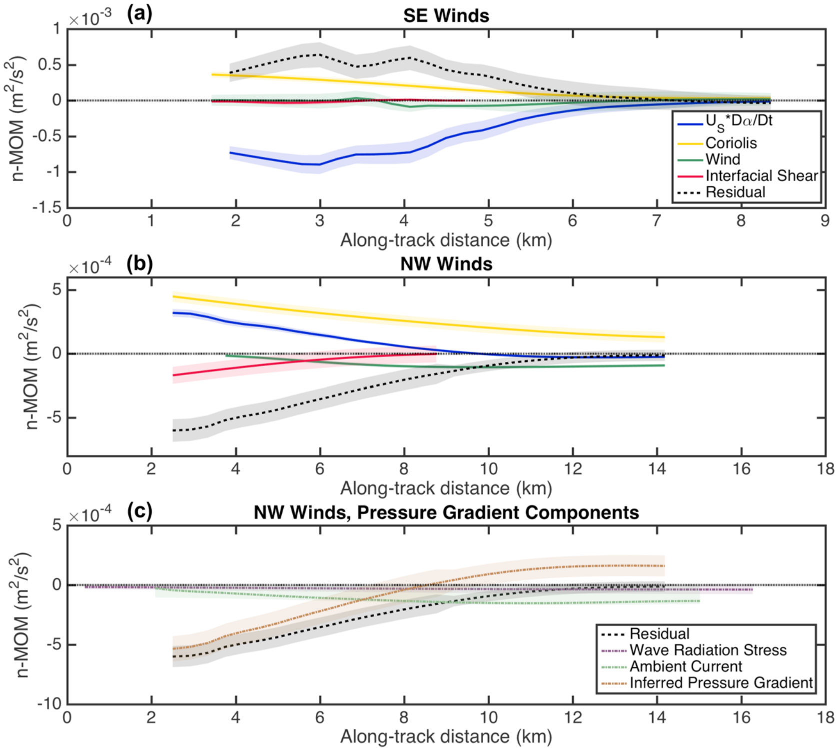

Figure 4. Along-track plots for depth-integrated terms in the stream-normal momentum equation for (a) SE winds (drifter pair S1) and (b) NW winds (drifter pair N1). (c) shows components of the pressure gradient for NW winds. The black-dotted line on (a)–(c) indicates zero momentum. Note that for SE winds, the maximum along-track distance is 8 km, and for NW winds, the maximum along-track distance is 15 km.

for longer which is consistent with the isohaline behavior and with numerical model results of a plume in a crossflow (O’Donnell, 1990). The surface flow does not decelerate as rapidly as under SE winds, reaching a final velocity of 1 m/s. Tidal and wind-driven currents flow underneath the surface river outflow. Under SE winds, observed currents beneath the plume (via shipboard ADCP measurements) show currents of 50 cm/s, while a downwind measurement from an AWAC mooring shows near-surface velocities of 20 cm/s. Under NW winds, observed currents beneath the plume (via shipboard ADCP measurements) show currents of 50 cm/s, while an upwind measurement from the AWAC mooring shows near-surface currents of 60 cm/s. The initial and end velocity and salinity profiles shown in Figure 3 are separated by about 2.5 hr under each wind condition.

Figure 3 shows that the Fraser plume does not behave like a classic two-layer slab model. For both wind conditions, the water is continuously stratified and sheared in the near field of the plume. Under SE winds, the plume evolves into a two-layer system in the far field, with a lower density layer persisting to 10-m depth and small continuous shear to 7-m depth. Under NW winds, a fresher surface layer persists to a depth of 2 m far from the river mouth, while continuous stratification and shear persist below this to a depth of approximately 10 m. However, the stratification and shear are of smaller magnitude than in the near field.

4.3. Stream-Normal Momentum Balance

Figure 4 shows the stream-normal momentum balance of one drifter pair for each wind condition (N1 for the NW winds and S1 for the SW winds) based on the calculations outlined in section 3.1 and equation (8). Under SE winds, the acceleration, Coriolis, and residual terms dominate the stream-normal momentum balance with minor contributions from the wind stress and interfacial shear stress terms (Figure 4a). We assume here that the residual is primarily a result of the pressure gradient, since wave breaking at the plume front and ambient current form drag are negligible due to the dominant wind and wave directions. Additionally, the observed decay in the residual away from the river mouth matches the expectations for the stream-normal pressure gradient from freshwater dome effect. Thus, as shown by Garvine (1987), MC09, and Chen et al. (2009), Coriolis and the pressure gradient combine to turn the plume to the right. This is consistent with the model of plume spreading laid out in MC09, in which each side of the freshwater dome has distinct stream-normal forcing due to the interaction of Coriolis and the pressure gradient. We will refer to these sides of the plume as the dynamical right and dynamical left side of the plume. On the dynamical right side of the plume, Coriolis and pressure gradient act in concert, resulting in a rightward acceleration and enhanced spreading. The magnitude of the terms becomes smaller over the course of the drift track as the plume momentum decays in space farther away from the river mouth.

Under NW winds (Figure 4b), the stream-normal momentum balance has other important terms; in addition to acceleration, Coriolis, and the residual, wind stress and interfacial shear stress also contribute. The balance of Coriolis with wind stress and interfacial shear stress results in a large net residual relative to the other terms and a smaller stream-normal acceleration than under SE winds. The residual is of the opposite sign as the residual under SE winds. As under SE winds, the residual includes the pressure gradient, but in this case, it also includes the terms M^n_{wave} and M^n_{ac}. Using the methods outlined in sections 3.1.1 and 3.1.2, we can estimate contributions to the pressure gradient from the wave radiation stress gradient and an ambient current form drag (Figure 4c). These quantities are small, but they do make a difference in the magnitude of the inferred pressure gradient compared to the residual.

Thus, under NW winds, the resulting stream-normal momentum balance of Coriolis and acceleration with wind stress, interfacial shear stress, wave radiation stress gradient, ambient current form drag, and inferred pressure gradient shows that the plume turns slightly to the left due to external forcing and the local pressure gradient. This is an example of the dynamical left side of the plume as described in MC09, as Coriolis and the pressure gradient act against each other to limit spreading. It should be noted that the wave radiation stress gradient is smaller than other terms under NW winds, with more significant terms contributing up to two orders of magnitude more to the momentum balance. We show in section 5.1 that the residuals lie in line with previous work, and so error is small relative to the signal of the pressure gradient term.

4.4. Spreading

Under SW winds, pair S1 initially displays spreading that is dominated by differences in drifter speed. As the drifters move offshore, angular spreading starts to become important. For pair S2, spreading is initially dominated by angular differences, but as the drifter moves offshore, differences in speed make up nearly all of the spreading. Due to the small total spreading observed by these drifters at the beginning of the drift track, the initial values of $B_\alpha/B_{\mathrm{tot}}$ are relatively noisy. This is reflected in the 95% confidence interval of the calculation, determined by propagating the error associated with fitting the drifter spreading. Under NW winds, pair N1 spreads in a similar manner to pair S2—initially low spreading dominated by the angular component, with differences in drift speed increasing in importance over the length of the drift track (Figures 5c and 5d). Pair N2 undergoes spreading similar to the right pair of drifters under SE winds, initially dominated by drift speed differences, with the influence of angular differences increasing over the length of the drift track. Pair N3 shows a different behavior, with angular spreading dominating early in the drift track, decreasing in value as the pair moves offshore.

Peak nondimensional spreading also varies both with wind condition and drifter release location. We define the nondimensional spreading parameter $\frac{B_0}{B}\frac{\partial B}{\partial s}$, where B_0 is the initial distance between drifters, to account for differences in initial drifter spacing. The differences in spreading rate are most pronounced in the initial 4 km of the drift tracks, where drifter pair S1 experiences a significant peak in the spreading rate compared with the minimal spreading rate observed for pair S2 (Figure 5e). Under NW winds, spreading rate seems to fall off from an initial peak, with pairs N3 and N3 having a higher spreading rate than pair N1 (Figure 5f). The spreading rate for pair S1 shuts down after its initial peak, while for pairs N1, N2, and N3, spreading rate slowly diminishes.

4.5. Mixing

Figures 5g and 5h show along-track mixing estimates for each pair of drifters. Drifter pair S1 observes vigorous mixing ($S_e w_e \approx 7 \times 10^{-2}$ psu m/s) at the beginning of the drift track and gradually stops mixing by $s \approx 4.5$ km. Pair S2 observes less intense, more consistent mixing throughout a similar track length. For both pairs S1 and S2, mixing has shut down by the point in the drift tracks where the plume has turned almost completely to the north. Drifter pairs N1, N2, and N3 observe similar mixing behavior to pair S2, with less intense, more consistent mixing persisting throughout much of the drift tracks. Mixing continues for a longer section of the drift track for pairs N2 and N3. Even so, the active mixing region is longer under NW winds than under SE winds. Mixing is more intense for pairs S2, N2, and N3 than for pair N1. The lower mixing rate under NW winds, where the plume is in a crossflow, is consistent with the predictions of O'Donnell (1990).

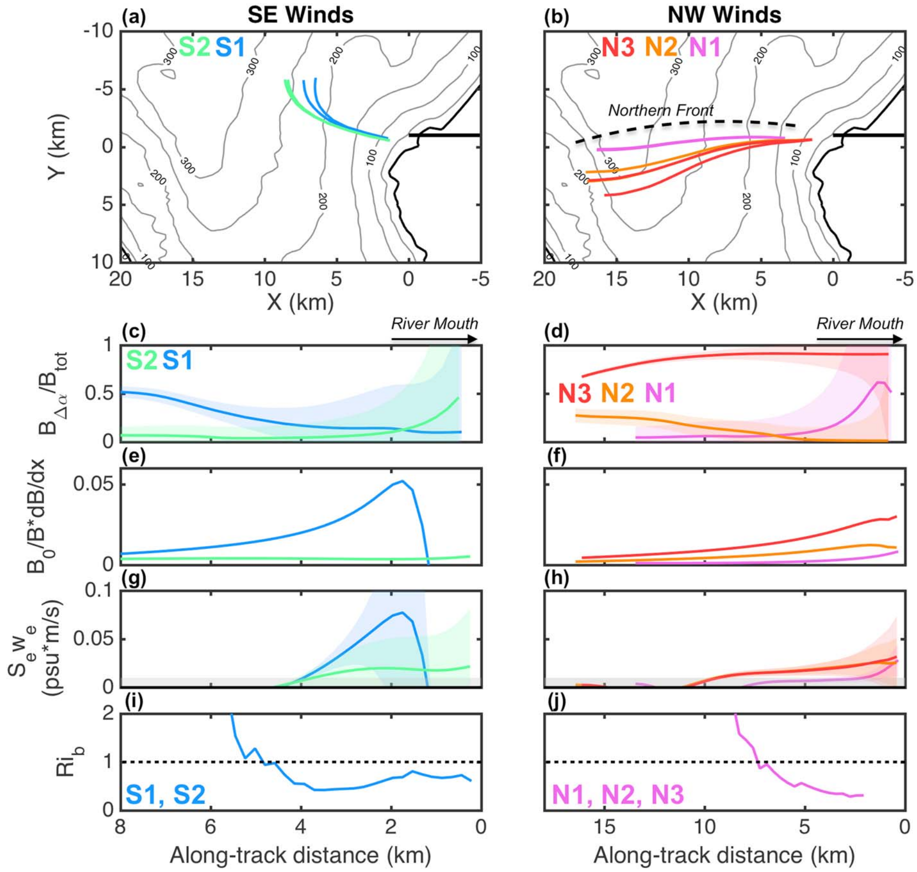

Figure 5. Spreading and mixing calculations for each wind condition and drifter pair. As in Figure 2, colors of drift tracks and along-track properties match for an indicated drifter pair. (a) and (b) show again the maps of drifter tracks over Strait of Georgia bathymetry, with drifter pair name indicated in the appropriate color. The thin solid black line is the western boundary of the tidal flats near Sand Heads. The thick solid black line is the Sand Heads jetty. An approximate northern front is notated as a black-dotted line on (b). (c) and (d) are along-track plots of the ratio of drift angle driven spreading over total spreading with 95% confidence intervals; (e) and (f) are along-track plots of nondimensional spreading rate; (g) and (h) are along-track plots of mixing rate as calculated using equation (10) with 95% confidence intervals; (i) and (j) are along-track plots of bulk Richardson number. Note that for SE winds, the maximum along-track distance is 8 km, and for NW winds, the maximum along-track distance is 15 km. For all along-track plots, along-track distance increases to the left to match the maps, with the river mouth at the origin on the right, as noted in (c) and (d). psu = practical salinity unit.

The salt flux values we obtain are roughly similar to previous studies. MC08 measured salt fluxes of up to 5×10^{-2} psu m/s at the Columbia, and MacDonald and Geyer (2004) measured salt flux of 1×10^{-1} psu m/s closer to the channel mouth in the Fraser; however, neither of these studies shows effects of mixing in the near field differing as a result of variable wind conditions. MC09 assumes the wind forcing does not have much influence on the plume momentum balance—this may be true for a system as energetic as the Columbia. However, the difference in the mixing behavior between the two days we have presented must either be associated with the change in wind direction or buoyancy input, as all other forcing conditions (Table 1) remained consistent between the two days. Since spreading seems to be the primary driver of mixing, and we have seen that spreading is reduced under NW winds due to the wind and ambient current, we therefore hypothesize that the wind forcing is primarily responsible for this change in mixing behavior.

Calculations of bulk Richardson number, $Ri_b = g'h_p/(\Delta u^2)$, are consistent with the salt flux results (Figures 5i and 5j). In these calculations, we take h_p as the depth of the 21 psu isohaline, Δu as the difference between SWIFT drift speed (to represent the plume velocity) and the velocity observed by a downlooking SWIFT just below the 21 psu isohaline (to represent the ambient velocity), ρ_p as the mean density above the 21 psu isohaline, and ρ_{ref} as 1,021 kg/m^3 (equivalent to water of 5 °C and 26 psu). We are able to make these calculations for drifter pairs S1 and N1, as these drifters were the nearest to the SWIFTv4β. Taking the critical value of bulk

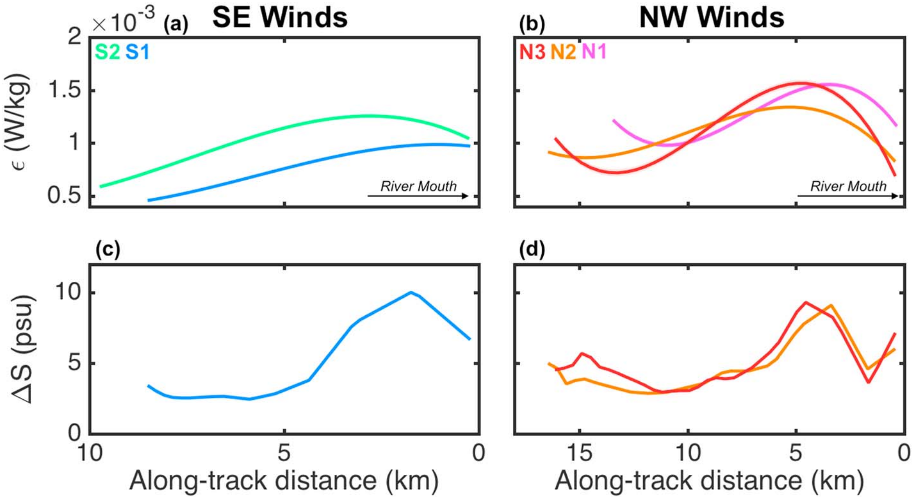

Figure 6. Near-surface salinity differences and dissipation plot along-track for each wind condition and drifter pair. Colors of along-track properties and drifter names match for a specific drifter pair. (a) and (b) are along-track plots of mean dissipation in the top 0.7 m of the water column; (c) and (d) show are along-track plots of the salinity difference in the top 1.2 m of the water column for Surface Wave Instrument Floats with Tracking with three CT sensors. Note that for SE winds, the maximum along-track distance is 8 km, and for NW winds, the maximum along-track distance is 15 km. For all along-track plots, along-track distance increases to the left to match the maps, with the river mouth at the origin on the right, as noted in (a) and (b).

Richardson number to be $Ri_c = 1$, we see that under NW winds, $Ri_b < 1$ at the beginning of the drift track; however, Ri_b rises through the drift track and exceeds Ri_c near the halfway point, indicating a shutdown of mixing as shown in salt flux calculations for drifter pair N1. We see similar behavior under SE winds for both pairs S1 and S2 (Figures 5i and 5j).

From SWIFTs with three CTs, we can see that the salinity difference between 0.2 and 1.2 m is similar for each wind condition at the beginning of the drift track (Figures 6c and 6d). By the end of the drifts, however, higher stratification persists under NW wind conditions than under SE wind conditions. Persistent higher stratification is consistent with our salt flux and bulk Richardson number calculations; less plume mixing occurs under NW wind conditions.

Average turbulent dissipation in the upper 0.7 m of the water column is higher for pairs N1, N2, and N3 than for pairs S1 and S2 (Figures 6a and 6b). This is likely due to the slightly higher wind velocities observed for NW wind conditions, as well as wave breaking that was apparent along the lateral northern front region of the plume from the deck of the *R/V Robertson*. Elevated turbulence with higher persistent stratification seems, at first, to be an incongruous observation; however, it falls in line with our above results showing that spreading is the primary driver of mixing in the system, as the turbulence present near the surface of the plume is not strong enough to contribute significantly to mixing below the surface.

5. Discussion

5.1. Consequences of Wind-Influenced Spreading

Our stream-normal momentum balance calculations show that wind-influenced terms and the pressure gradient stop the plume from spreading under NW winds. The effects of wind stress, interfacial shear stress, and ambient current form drag are relatively straightforward to understand, as these are all external forces that push or drag on the plume. The ambient current and its associated interfacial shear stress are important to the stream-normal momentum balance under NW winds because it is only for this wind condition that they are normal to the plume streamlines for the majority of the drift track. The combination of these two currents creates a strong near-surface flow in the Strait that collides with the plume and subducts under it, imparting a form drag on the lateral plume front in the process. This form drag is partially compensated by a baroclinic pressure gradient at the front associated with frontal tilt and causes interfacial shear stress as it subducts (O'Donnell et al., 1998). Under SE winds, the wind stress and its associated current oppose the ebb tidal velocity, which should result in slower near-surface flow; we lack observations south of the plume to corroborate this hypothesis. Additionally, the ebb tidal flow out of the NW would be incorporated in the

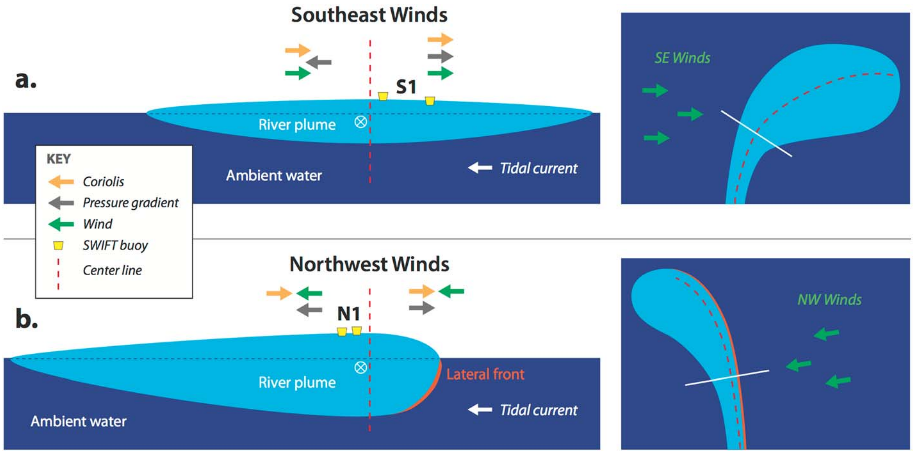

Figure 7. Cross-sectional and plan view schematics of the two plume conditions observed. (a) shows SE winds, and (b) shows northwest winds. The red-dashed lines in all panels indicate the plume centerline (vertically in cross sections, streamwise in plan views). Arrows indicate the direction of stream-normal momentum balance terms on either dynamical half of the plume. White lines on the plan view schematics indicate the cross-section position. The approximate positions of SWIFT pairs S1 and N1 are indicated by the SWIFT markers on the cross-sectional schematic. These schematics are not to scale. SWIFT = Surface Wave Instrument Float with Tracking.

streamwise momentum balance once the plume turns under SE wind influence and thus would not increase the stream-normal interfacial shear stress after that point.

Like MC09, we see varied spreading behavior between our drifter pairs, particularly in the components of spreading that are important over the course of a pair of drift tracks. MC09 differentiate between plume spreading behavior on either side of the freshwater dome. On the right side of the dome, plume spreading is caused by both differences in streamline angle between streamlines ($B_{\Delta\alpha}$) and stream-normal differences in the streamwise momentum balance ($B_{\Delta U}$). This is the dynamical right side of the plume, where Coriolis and the pressure gradient align to cause an angular acceleration to the right. On the left side of the dome, plume spreading is primarily caused by $B_{\Delta U}$. This is the dynamical left side of the plume, where Coriolis and the pressure gradient oppose each other to limit the angular acceleration. Thus, by calculating the ratio $B_{\Delta\alpha}/B_{\text{tot}}$ and analyzing the momentum balance of different drifter pairs, we can determine which dynamical side of the plume the drifter pair traverses (Figures 5c and 5d). Recall that the drifter sampling protocol was the same under both SE and NW winds: pairs of drifters were deployed at different cross-channel positions.

Under SE winds, pair S1 was originally deployed in the center of the channel. These drifters show a contribution to spreading from $B_{\Delta\alpha}$, and they exhibit an alignment of Coriolis and pressure gradient causing a rightward angular acceleration, consistent with our expectations of the dynamical right side of the plume. Drifter pair S2 was originally deployed on the left side of the channel. These drifters show minimal contribution to spreading from $B_{\Delta\alpha}$ further in their drift track and limited spreading. Although we are not able to make momentum balance calculations for this pair of drifters, the limited spreading dominated by differences in speed suggests that this drifter pair is on the dynamical left side of the plume. The centerline of the plume, and the largest sea surface height anomaly associated with the freshwater dome, can be inferred to be located between these two drifter pairs (Figure 7a). By inferring the location of the plume centerline, we gain knowledge of the overall shape of the sea surface height anomaly associated with the freshwater dome.

Under NW winds, drifter pair N1 was originally deployed on the right side of the channel. These drifters experience a minimal contribution to spreading from $B_{\Delta\alpha}$, and the momentum balance shows a competition between Coriolis and the pressure gradient (along with the wind) causing a slight leftward acceleration, consistent with our expectations of the dynamical left side of the plume. As drifter pair N1 is on the left side of the plume, the plume centerline must lie to its right. The northern plume front was also observed very close to this northernmost pair of drifters, indicating that the dynamical right side of the plume is narrower under NW winds than under SE winds. Under SE winds, a drifter pair released in the center of the channel ends up on the right side of the plume, and under NW winds, a drifter pair released on the right side of the channel ends up on the left side of the plume.

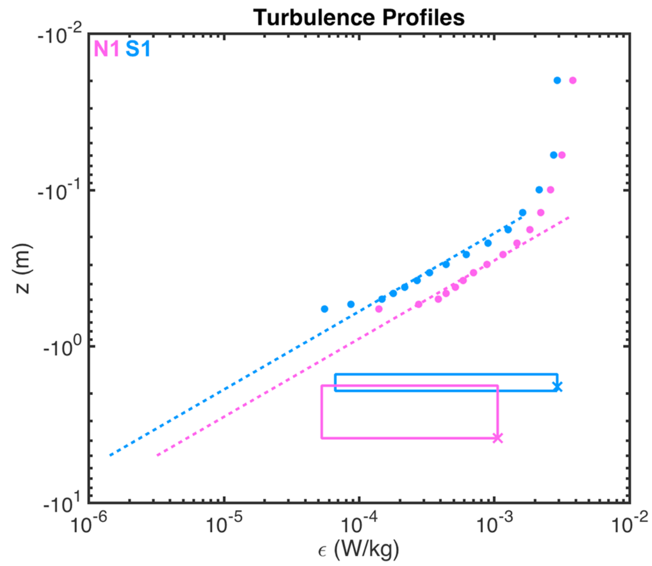

Figure 8. Mean dissipation profiles from the indicated drifter pairs. The points indicate the mean dissipation at a certain depth measured by the drifters with uplooking acoustic Doppler current profilers in the pair. The dashed lines indicate the fit to these profiles given by equation (12). The solid boxes indicate the range of plume depths and dissipation values ϵ^{salt} calculated in the plume mixing area for each drifter pair, with the "X" on the box indicating the magnitude and depth of the maximum dissipation calculated.

Drifter pairs N2 and N3 were originally deployed in the middle and left positions in the channel, respectively. These drifters experience a large contribution to spreading from $B_{\Delta\alpha}$. Their nondimensional spreading is larger than pairs S2 and N1 and similar in magnitude to S1 after its initial peak. Such spreading behavior would normally indicate that these drifters are on the dynamical right side of the plume; however, they are to the left of a drifter pair that is definitively on the left side of the plume. Pairs N2 and N3 also turn slightly to the left initially, indicating that Coriolis is not a dominant factor in the initial dynamics of the plume (Figure 2b). The terms that could be causing this leftward acceleration are thus the pressure gradient, ambient current, and the wind stress. It is possible that the pressure gradient is of a stronger magnitude farther to the left in the plume, indicating a steeper sea surface slope. The leftward turning, opposite of Coriolis, also indicates that these drifters are on the dynamical left side of the plume. Thus, under NW winds, the dynamical left side of the plume takes up most of the plume area, as drifters released in all channel mouth positions show characteristics of the left side of the plume (Figure 7b). The dynamical right side of the plume occupies the space between the plume centerline and the front, both of which are to the right of the northernmost pair of drifters. Thus, the freshwater dome, present under SE winds, has been altered by the wind condition to include mostly its left side. This is analogous to the findings of Garvine (1982), in which plume volume flux is concentrated near a lateral front due to a deepening of the plume interface in the vicinity of the front. We would expect this effect to be larger in practice than in Garvine's analytical model, as the inclusion of rotation would only enhance the channelization effect due to the ambient current, as the plume becomes sandwiched between the two forces. Figure 7 shows a schematic of the plume behavior under each wind condition. It follows that large-scale reshaping of the plume has a large effect on mixing.

Mixing in a plume is classically described as a competition between spreading and shear-driven turbulence (Garvine, 1984; Hetland, 2010), which is encapsulated by the Richardson number. As the plume leaves the river mouth, its high velocity relative to the ambient water drives shear instabilities, which in turn decrease this velocity. Concurrently, the plume spreads, increasing its velocity and its surface area available for mixing. These two processes simultaneously act to either decelerate or accelerate the plume and, in balance, would hold the Richardson number at a critical value. Once one process dominates the other, the Richardson number increases, and the plume stops mixing. Under SE winds, we observe $Ri_b < 1$ for half of the drift track, which is consistent with our observations of salinity in the upper water column. At the beginning of the drift track, spreading drives intense mixing until the fresher river water is substantially mixed into the ambient Strait of Georgia water (Figures 5e–5h). Under NW winds, lower spreading values lead to smaller salt fluxes over a larger along-track distance with $Ri_b < 1$. From our results, it seems that local plume mixing rates are higher on the right side of the plume than the left. MC09 shows consistent results, with lower salt fluxes to the left side of the plume, although the dynamical side of the plume is not explicitly determined. More work is required to generalize this theory.

5.2. Role of Waves

Our momentum balance does not indicate a significant contribution from wave breaking momentum. We next consider whether TKE from wave breaking is important to mixing. We compare measured near-surface TKE dissipation rate (from SWIFTs with uplooking ADCPs) extrapolated to the depth of the 21 psu isohaline using a scaling from Terray et al. (1996) to a calculated TKE dissipation rate based on salt flux. The calculated TKE dissipation rate is derived from the previously calculated salt flux by assuming a mixing efficiency (equation (11). We define the extrapolated dissipation rate, ϵ^{wave} by assuming the near-surface dissipation measured by the SWIFT is all due to wave breaking. Terray et al. (1996) define the following scaling:

$$\epsilon^{\mathrm{wave}}(z)H_{\mathrm{sig}} = G(\frac{z}{H_{\mathrm{sig}}})^{-2}, \quad (12)$$

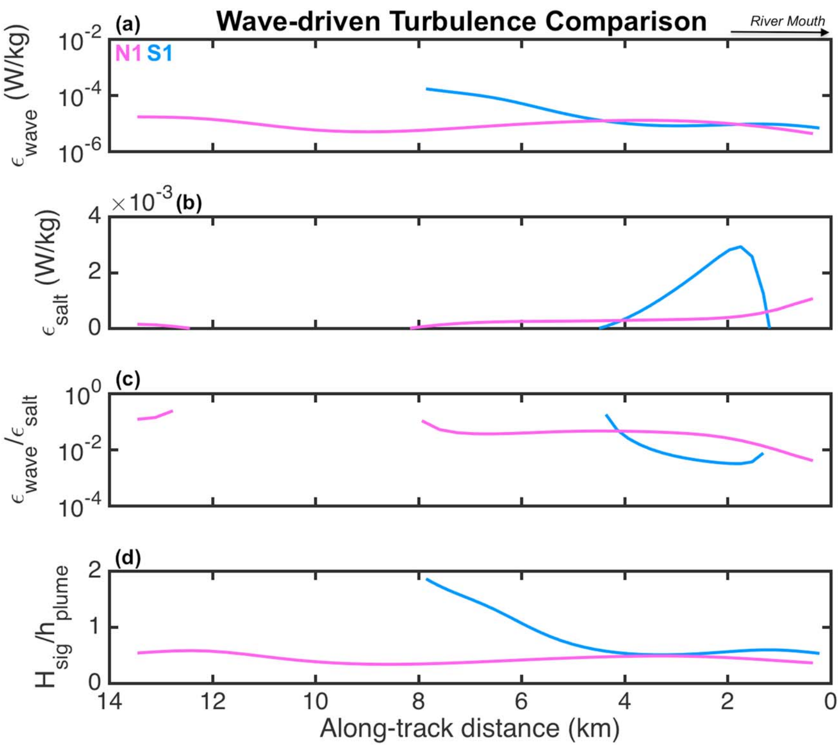

Figure 9. Wave- and spreading-driven turbulence for each wind condition. Colors of along-track properties and drifter names match for a specific drifter pair. Along-track plots for (a) dissipation extrapolated from near-surface Surface Wave Instrument Float with Tracking measurements to the base of the plume in watt per kilogram; (b) dissipation associated with salt flux through the base of the plume in watt per kilogram; (c) the ratio of (b) to (a); (d) the ratio of plume depth to significant wave height. Note that for SE winds, the maximum along-track distance is 8 km, and for NW winds, the maximum along-track distance is 15 km. For all along-track plots, along-track distance increases to the left to match the maps, with the river mouth at the origin on the right, as noted in (a).

where G is a parameter representing the flux of turbulence through the surface that we determine by fitting $(z/H_{\text{sig}})^{-2}$ to each 10-min average SWIFT uplooking turbulent dissipation rate profile and represents the surface input of turbulence (Figure 8; Craig & Banner, 1994; Terray et al., 1996; Thomson et al., 2016. Using the depth of the 21 psu isohaline for z in equation (12) gives the value of wave-driven dissipation at the interface, ϵ_i^{wave}. ϵ_i^{wave} is dependent on both the value of G and the depth of the isohaline, but the along-track variability of ϵ_i^{wave} closely follows that of the 21 psu isohaline depth for both wind conditions. Thus, the isohaline depth is the dominant term in determining the value of ϵ_i^{wave} and therefore the relative importance of wind/wave mixing at the base of the plume. Figure 9a shows along-track values of ϵ_i^{wave}, with values increasing from $\mathcal{O}(10^{-4})$ to $\mathcal{O}(10^{-3})$ W/kg for SE winds and remaining within $\mathcal{O}(10^{-5})$ W/kg for NW winds.

To calculate the dissipation associated with the calculated salt flux through the 21 psu isohaline, ϵ^{salt}, we use equation (11). The value ϵ^{salt} is thus the total dissipation (from any turbulent source) required to generate the observed salt flux. Figure 9b shows the along-track results from this calculation, which show peak ϵ^{salt} values of 2×10^{-3} W/kg under SE winds and peak values of 5×10^{-4} W/kg under NW winds. As the dissipation is directly proportional to the salt flux, the two quantities have identical along-track variability. Figure 8 shows the wave-driven near-surface turbulence, its expected decay from equation (12), the range of calculated values for ϵ^{salt}, and the depths these dissipation values are associated with. In general, values of *epsilon*$^{\text{salt}}$ are at least two orders of magnitude higher than *epsilon*$^{\text{wave}}$ at a similar depth.

The ratio $\epsilon_i^{\text{wave}}/\epsilon^{\text{salt}}$ provides an estimate of the relative contribution of wave-driven mixing to the observed mixing at the base of the plume (Figure 9c). By this measure, there is no evidence of a significant wave impact on plume mixing for either SE or NW conditions. For the beginning of each drift track, ϵ_i^{wave} makes up 1% to 5% of the total dissipation calculated in the near-field region where $Ri_b < 1$ (Figure 9c). Based on the dependence of $\epsilon_i^{\text{waves}}$ with the depth of the 21 psu isohaline, the regions of significant mixing under each wind condition are too deep for turbulence from wave breaking to significantly impact mixing. For the portions of the drift tracks where $S_e w_e > 0$, we find that the plume is at least two wave-heights thick ($h_p/H_{\text{sig}} \geq 2$; Figure 9d). In the open ocean, wave-driven turbulent transport balances dissipation in the TKE budget to a depth of approximately $10H_{\text{sig}}$ (Gerbi et al., 2009; Terray et al., 1996). Our shallower depth limit for wave-dominated turbulence suggests that there must be influence from the buoyancy or shear production terms in the TKE budget, which we would expect in the presence of strongly stratified surface shear layer such as a river plume.

Our results suggest that h_p/H_{sig} determines the influence of wave-driven turbulence on mixing in the plume. To estimate the critical value of h_p/H_{sig} where wave-driven turbulence becomes important to plume mixing, we must first assume a plume-following reference frame where the plume depth does not respond to forcing from the wave orbital velocities and stays locally constant relative to wave-averaged sea level. We can then leverage equation (12) to calculate $H_{\text{sig}}^{\text{eff}}$, the value of H_{sig} for which ϵ_i^{wave} is significant compared to $epsilon^{\text{salt}}$. Assuming that this would occur at a value $eps_i^{\text{wave}} = 0.2 * eps^{\text{salt}}$, we rearrange equation (12) to solve for $H_{\text{sig}}^{\text{eff}}$. To make this calculation, we must assume that all waves breaking and causing surface turbulence are wind waves. A classic approach parameterizes the surface turbulent flux $G = \alpha u_*^3$ for whitecapping of wind waves Craig and Banner (1994). We can thus use empirical fetch laws to parameterize G in terms of H_{sig} rather than u_*. Assuming a fully developed sea state, we find

$$G = \alpha \left(\frac{g H_{\text{sig}}}{\hat{H}_F} \right)^{3/2}, \tag{13}$$

where the constant $\alpha = 75$ and the fully developed nondimensional wave height $\hat{H}_F = 211.5$ (Pierson & Moskowitz, 1964; Thomson et al., 2016). Using the maximum calculated values of eps^{salt} for drifter pairs S1 and N1 and the corresponding measured values of h_p yields a value of $H_{\text{sig}}^{\text{eff}} = 1.42$ m for pair S1 ($H_{\text{sig}}/h_p^{\text{eff}} = 0.77$) and $H_{\text{sig}}^{\text{eff}} = 1.74$ m for pair N1 ($H_{\text{sig}}/h_p^{\text{eff}} = 0.45$). These are each approximately 30% larger than the measured wave heights. This simple model likely underpredicts $H_{\text{sig}}^{\text{eff}}$, as the observed value of ϵ_i^{wave} is approximately 2–4% of the values used as inputs for $epsilon_i^{\text{wave}}$ in the calculation. Thus, under stronger wave forcing, it could be possible for wave-driven turbulence to contribute to plume mixing, although more work is required to properly constrain this calculation.

Based on Thomson et al. (2014), we expected the plume current to cause measurable wave breaking. We visually observed vigorous breaking along the lateral northern front (and noticed a band in the ship's radar). However, the plume current had little effect on total wave energy, which is likely because the wave breaking was limited to the high frequency portion of the wave spectrum. Future work could likely refine the simple model above by using a formulation for the surface turbulent flux $G = \frac{\partial}{\partial x}(E c_g)$, where E is the wave energy and c_g is the group velocity. This formulation more appropriately describes the spatial change in the wave energy flux likely to observed at a river plume front. In general, the observed nondimensional wave energy scaled with nondimensional fetch as in Kahma (1981), without clear changes at the plume front (not shown). The plume current did have an expected effect on wave steepness. Opposing currents under NW winds increased wave steepness, and following currents under SE winds decreased wave steepness (also not shown).

5.3. Net Mixing

We observe higher local mixing rates under SE winds but more persistent mixing under NW winds. Thus, it is valuable to compare the net mixing rates experienced by drifter pairs over the course of their deployment. This net mixing rate, Q_{salt}, is calculated according to

$$Q_{\text{salt}} = \Sigma_i A_i \times (S_e w_e)_i, \tag{14}$$

where A_i is the trapezoidal area traced by drifters over a 10-min SWIFT data collection burst, and $(S_e w_e)_i$ is the salt flux calculated over A_i. We calculate this net mixing rate over the entire initial region where $S_e w_e > 0$. Figure 10 shows the peak mixing and net mixing calculation for each drifter pair. Uncertainty from the mixing calculation is shown as a 95% confidence interval for the net mixing. Under SE winds, we see low net mixing, as the high mixing rates for pair S1 do not act over a large area (Figures 10a and 10c). Under NW winds, the lower mixing rates persist for a larger portion of drifts N2 and N3, leading to larger net mixing for these drifter pairs than under SE winds (Figures 10b and 10d). Drifter pair N1 under NW winds experiences less net mixing as the smaller local mixing occurs over a smaller area than pairs N2 and N3. Using the length of the mixing region measured by N1 in the net mixing calculation for N2 and N3 lowers the net mixing value for pairs N2 and N3 but does not reduce their net mixing values below that of pair S1.

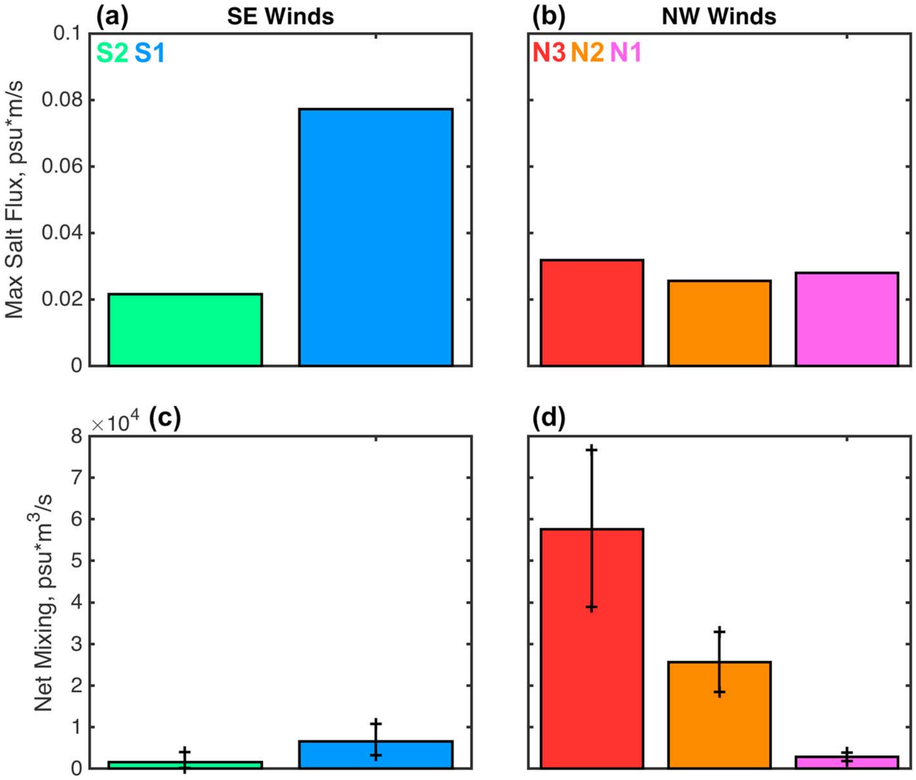

Figure 10. Maximum local salt flux and net mixing calculated for each drifter pair. Colors of plotted properties and drifter names match for a specific drifter pair. (a) and (b) show the maximum salt flux calculated over each drift track using equation (10); (c) and (d) show the net mixing over the length of the drift track calculated using equation (14). Black lines and crosses indicate the 95% confidence interval of the net mixing calculation. psu = practical salinity unit.

The overall higher mixing under NW winds indicates that the wind-driven alteration of the plume momentum balance, spreading, and local mixing rates can have an effect on the net mixing of the plume in different regions by either decreasing local mixing or increasing the length of the mixing area. The longer mixing area is caused by higher drift velocities persisting farther offshore, which is the result of the plume channelization and limited plume spreading described in section 5.1. Thus, a larger active mixing region can compensate for small local salt fluxes and result in a similar or larger cumulative value of Q_{salt} for the two different wind conditions. This is similar to the findings of Yuan and Horner-Devine (2013), who determined that the area of the base of the plume is a key factor in plume mixing. Despite this similarity, it is counterintuitive that there would be more net mixing under NW winds, when there is less spreading, as we would expect the loss of momentum due to shear instabilities to increase the Richardson number above a critical value and shut down mixing. Mixing clearly persists, indicating that the shear required to generate the smaller salt fluxes observed along track under NW winds is not large enough to increase the Richardson number above critical until at least 8 km into the drift track (for pair N1).

6. Summary

We have shown that under two different wind conditions, we observe different behavior, mixing, and dynamics in the near-field Fraser River plume on an ebbing tide. Under SE winds, the plume spreads, thins, turns to the right, and mixes intensely due to a stream-normal momentum balance dominated by rotational acceleration, pressure gradient, and Coriolis. Under NW winds, the plume spreads less and remains thicker while propagating directly across the Strait of Georgia, mixing less intensely. A stream-normal momentum balance shows this behavior is due to a combination of wind stress, an ambient current in the Strait, interfacial shear stress, and pressure gradient opposing Coriolis. These opposing forces sandwich the plume, preventing it from mixing intensely. We observe wave contributions to mixing and momentum over the whole surface layer to be small, although somewhat larger near-surface turbulence is observed under NW wind conditions. Calculations of the causes of plume spreading show that under NW wind conditions, the wind can reconfigure the plume such that the dynamical left side of the plume takes up most of the plume area. The longer zone of active mixing under NW winds results in a larger cumulative volumetric salt flux into the plume despite lower salt fluxes per unit area, indicating that the area of the region of active mixing plays a key role in the net mixing of the plume.

Acknowledgments
The authors would like to acknowledge NSF grant OCE-1459051 for providing funding for this project. Nirnimesh Kumar (UW) provided constructive critiques of this work, and Rich Pawlowicz and Mark Halvorsen (UBC) provided helpful local knowledge. The observational program would not have been possible without the technical expertise of Joe Talbert, Alex DeKlerk, and Captain Andy Reay-Ellers of the University of Washington Applied Physics Lab. Kim Reading (UW-APL) contributed the schematic for Figure 7. Data are available at apl.uw.edu/SWIFT.

References

Akan, C., Moghimi, S., Özkan-Haller, H, Osborne, J., & Kurapov, A. (2017). On the dynamics of the mouth of Columbia River: Results from a three-dimensional fully coupled wave-current interaction model. *Journal of Geophysical Research: Oceans*, *122*, 2373–2388. https://doi.org/10.1002/2016JC012307

Banner, M. L., Babanin, A. V., & Young, I. (2000). Breaking probability for dominant waves on the sea surface. *Journal of Physical Oceanography*, *30*, 3145–3160.

Chao, S. (1988a). River-forced estuarine plumes. *Journal of Physical Oceanography*, *18*, 72–88.

Chao, S. (1988b). Wind-driven motion of estuarine plumes. *Journal of Physical Oceanography*, *18*, 1144–1166.

Chawla, A., & Kirby, J. T. (2002). Monochromatic and random wave breaking at blocking points. *Journal of Geophysical Research*, *107*(C7), 3067.

Chen, F., MacDonald, D. G., & Hetland, R. D. (2009). Lateral spreading of a near-field river plume: Observations and numerical simulations. *Journal of Geophysical Research*, *114*, C07013. https://doi.org/10.1029/2008JC004893

Craig, P., & Banner, M. (1994). Modeling wave-enhanced turbulence in the ocean surface layer. *Journal of Physical Oceanography*, *24*(12), 2546–2559.

Csanady, G. T (1978). The arrested topographic wave. *Journal of Physical Oceanography*, *8*, 47–62.

Feddersen, F. (2012). Scaling surf zone turbulence. *Geophysical Research Letters*, *39*, L18613. https://doi.org/10.1029/2012GL052970

Fong, D. A., & Geyer, W. R. (2001). Response of a river plume during an upwelling favorable wind event. *Journal of Geophysical Research*, *106*(C1), 1067–1084.

Fong, D. A., Geyer, W. R., & Signell, R. P. (1997). The wind-forced response of a buoyant coastal current: Observations of the western Gulf of Maine. *Journal of Marine Systems*, *12*, 69–81.

Garvine, R. W. (1982). A steady state model for buoyant surface plume hydrodynamics in coastal waters. *Tellus*, *34*, 293–306.

Garvine, R. W. (1984). Radial spreading of buoyant, surface plumes in coastal waters. *Journal of Geophysical Research*, *89*(C2), 1989–1996.

Garvine, R. W. (1987). Estuary plumes and fronts in shelf waters: A layer model. *Journal of Physical Oceanography*, *17*, 1877–1896.

Gemmrich, J. (2010). Strong turbulence in the wave crest region. *Journal of Physical Oceanography*, *40*, 583–595. https://doi.org/10.1175/2009JPO4179.1

Gerbi, G. P., Chant, R. J., & Wilkin, J. L. (2013). Breaking surface wave effects on river plume dynamics during upwelling-favorable winds. *Journal of Physical Oceanography*, *43*, 1959–1980.

Gerbi, G., Kastner, S. E., & Brett, G. (2015). The role of whitecapping in thickening the ocean surface boundary layer. *Journal of Physical Oceanography*, *45*(8), 2006–2024.

Gerbi, G. P., Trowbridge, J. H., Terray, E. A., Plueddemann, A. J., & Kukulka, T. (2009). Observations of turbulence in the ocean surface boundary layer: Energetics and transport. *Journal of Physical Oceanography*, *39*(5), 1077–1096.

Geyer, W. R., Ralston, D. K., & Holleman, R. C. (2017). Hydraulics and mixing in a laterally divergent channel of highly stratified estuary. *Journal of Geophysical Research: Oceans*, *122*, 4743–4760. https://doi.org/10.1002/2016JC012455

Hench, J. L., & Leuttich, R. A. (2003). Transient tidal circulation and momentum balances at a shallow inlet. *Journal of Physical Oceanography*, *33*(4), 913–932.

Hetland, R. D. (2005). Relating river plume structure to vertical mixing. *Journal of Physical Oceanography*, *35*(9), 1667–1688.

Hetland, R. D. (2010). The effects of mixing and spreading on density in near-field river plumes. *Dynamics of Atmospheres and Oceans*, *49*, 37–53. https://doi.org/10.1016/j.dynatmoce.2008.11.003

Hickey, B. M., Pietrafesa, L. J., Jay, D. A., & Boicourt, W. C. (1998). The Columbia River Plume Study: Subtidal variability in the velocity and salinity fields. *Journal of Geophysical Research*, *103*(C5), 10,339–10,368.

Horner-Devine, A., Hetland, R. D., & MacDonald, D. (2015). Transport and mixing in coastal river plumes. *Annual Review of Fluid Mechanics*, *47*, 569–594.

Horner-Devine, A. R., Jay, D., Orton, P., & Spahn, E. (2009). A conceptual model of the strongly tidal Columbia River plume. *Journal of Marine Systems*, *78*, 460–475.

Houghton, R. W., Tilburg, C. E., Garvine, R. W., & Fong, A. (2004). Delaware River plume response to a strong upwelling-favorable wind event. *Geophysical Research Letters*, *31*, L07302. https://doi.org/10.1029/2003GL018988

Hunter, E. J., Chant, R. J., Wilkin, J. L., & Kohut, J. (2010). High-frequency forcing and subtidal response of the Hudson River plume. *Journal of Geophysical Research*, *115*, C07012. https://doi.org/10.1029/2009JC005620

Jurisa, J. T., Nash, J. D., Moum, J. M., & Kilcher, L. (2016). Controls on turbulent mixing in a strongly stratified and sheared tidal river plume. *Journal of Physical Oceanography*, *46*(8), 2373–2388.

Kahma, K. K. (1981). A study of the growth of the wave spectrum with fetch. *Journal of Physical Oceanography*, *11*(11), 1503–1515.

Kakoulaki, G., MacDonald, D., & Horner-Devine, A. (2014). The role of wind in the near field and midfield of a river plume. *Geophysical Research Letters*, *41*, 5132–5138. https://doi.org/10.1002/2014GL060606.

Kilcher, L., Nash, J., & Moum, J. N. (2012). The role of turbulence stress divergence in decelerating a river plume. *Journal of Geophysical Research*, *117*, C05032. https://doi.org/10.1029/2011JC007398

Lentz, S (2004). The response of buoyant coastal plumes to upwelling-favorable winds. *Journal of Physical Oceanography*, *34*(11), 2458–2467.

Lentz, S. J., & Largier, J. (2006). The influence of wind forcing on the Chesapeake Bay buoyant coastal current. *Journal of Physical Oceanography*, *36*(7), 1305–1316.

Longuet-Higgins, M. S. (1970). Longshore currents generated by obliquely incident sea waves: 1. *Journal of Geophysical Research*, *75*(33), 6778–6789.

Longuet-Higgins, M., & Stewart, R. (1961). The changes in amplitude of short gravity waves on steady non-uniform currents. *Journal of Fluid Mechanics*, *10*(4), 529–543.

Longuet-Higgins, M., & Stewart, R. (1962). Radiation stress and mass transport in gravity waves, with application to ‘surf beats’. *Journal of Fluid Mechanics*, *13*(4), 481–504.

Luketina, D., & Imberger, J. (1987). Characteristics of a surface buoyant jet. *Journal of Geophysical Research*, *92*(C5), 5435–5447.

Luketina, D., & Imberger, J. (1989). Turbulence and entrainment in a buoyant surface plume. *Journal of Geophysical Research*, *94*(C9), 12,619 – 12,636.

MacDonald, D. G., & Chen, F. (2012). Enhancement of turbulence through lateral spreading in a stratified-shear flow: Development and assessment of a conceptual model. *Journal of Geophysical Research*, *117*, C05025. https://doi.org/10.1029/2011JC007484

MacDonald, D. G., & Geyer, W. R. (2004). Turbulent energy production and entrainment at a highly stratified estuarine front. *Journal of Geophysical Research*, *109*, C05004. https://doi.org/10.1029/2003JC002094

MacDonald, D. G., & Geyer, W. R. (2005). Hydraulic control of a highly stratified estuarine front. *Journal of Physical Oceanography*, *35*, 374 – 387. https://doi.org/10.1029/2003JC002094

MacDonald, D. G., Goodman, L., & Hetland, R. D. (2007). Turbulent dissipation in a near-field river plume: A comparison of control volume and microstructure observations with a numerical model. *Journal of Geophysical Research*, *112*, C07026. https://doi.org/10.1029/2006JC004075

Masse, A., & Murthy, C. R. (1990). Observations of the Niagara River thermal plume (Lake Ontario, North America). *Journal of Geophysical Research*, *95*(C9), 16,097 – 16,109.

McCabe, R., Hickey, B. M., & MacCready, P. (2008). Observational estimates of entrainment and vertical salt flux in the interior of a spreading river plume. *Journal of Geophysical Research*, *113*, C08027. https://doi.org/10.1029/2007JC004361

McCabe, R., MacCready, P., & Hickey, B. M. (2009). Ebb-tide dynamics and spreading of a large river plume. *Journal of Physical Oceanography*, *39*(11), 2839 – 2856.

Mei, C. (1989). *The applied dynamics of ocean surface waves, advanced series on ocean engineering* (Vol. 1). Singapore: World Scientific.

Melville, W. K (1996). The role of surface-wave breaking in air-sea interaction. *Annual Review of Fluid Mechanics*, *28*, 279 – 321.

O'Donnell, J. (1990). The formation and fate of a river plume: A numerical model. *Journal of Physical Oceanography*, *20*(4), 551 – 569.

O'Donnell, J., Marmorino, G. O., & Trump, C. L. (1998). Convergence and downwelling at a river plume front. *Journal of Geophysical Research*, *28*, 1481 – 1495.

Paris, M. G., & Thomson, J. (2017). Turbulence measurements from 5-beam acoustic Doppler current profilers. *Journal of Atmospheric and Oceanic Technology*, *34*, 1267 – 1284. https://doi.org/10.1175/ JTECH-D-16-0148.1

Peltier, W. R., & Caulfield, C. P. (2003). Mixing efficiency in stratified shear flows. *Annual Review of Fluid Mechanics*, *35*(1), 135 – 167.

Pierson, W. J., & Moskowitz, L. (1964). A proposed spectral form for fully developed wind seas based on the similarity theory of A. A. Kitaigorodskii. *Journal of Geophysical Research*, *69*, 5181 – 5190.

Rong, Z., Hetland, R. D., Zheng, W., & Zhang, X. (2014). Current-wave interaction in the Mississippi-Atchafalaya River plume on the Texas-Louisiana Shelf. *Ocean Modelling*, *84*(1), 67 – 83.

Terray, E. A., Donelan, M. A., Agrawal, Y. C., Drennan, W., Kahma, K. K., Williams, A. J., et al. (1996). Estimates of kinetic energy dissipation under breaking waves. *Journal of Physical Oceanography*, *26*(5), 792 – 807.

Thomson, J. (2012). Wave breaking dissipation observed with SWIFT drifters. *Journal of Atmospheric and Oceanic Technology*, *29*(12), 1866 – 1882.

Thomson, J., Horner-Devine, A. R., Zippel, S., Rusch, C., & Geyer, W. (2014). Wave breaking turbulence at the offshore front of the Columbia River plume. *Geophysical Research Letters*, *41*, 8987 – 8993. https://doi.org/10.1002/2014GL062274

Thomson, J., Schwendeman, M. S., Zippel, S. F., Moghimi, S., Gemmrich, J., & Rogers, W. E. (2016). Wave-breaking turbulence in the ocean surface layer. *Journal of Physical Oceanography*, *46*(6), 1857 – 1870. https://doi.org/10.1175/JPO-D-15-0130.1

Thornton, E. B., & Guza, R. T. (1986). Surf zone longshore currents and random waves: Field data and models. *Journal of Physical Oceanography*, *16*(7), 1165 – 1178.

Wright, L. D., & Coleman, J. M. (1971). Effluent expansion and interfacial mixing in the presence of a Salt Wedge, Mississippi River Delta. *Journal of Geophysical Research*, *76*(36), 8649 – 8661.

Yuan, Y., & Horner-Devine, A. (2013). Laboratory investigation of the impact of lateral spreading on buoyancy flux in a river plume. *Journal of Physical Oceanography*, *43*(12), 2588 – 2610.

Yuan, Y., & Horner-Devine, A. R. (2017). Experimental investigation of large-scale vortices in a freely spreading gravity current. *Physics of Fluids*, *29*(10), 106603.

Zippel, S., & Thomson, J. (2015). Wave breaking and turbulence at a tidal inlet. *Journal of Geophysical Research: Oceans*, *120*, 1016 – 1031. https://doi.org/10.1002/2014JC010025

Zippel, S., & Thomson, J. (2017). Surface wave breaking over sheared currents: Observations from the mouth of the Columbia River. *Journal of Geophysical Research: Oceans*, *122*, 3311 – 3328. https://doi.org/10.1002/2016JC012498